Sha, Mo; Liu, Long; Zhao, Huaping; Lei, Yong:

Anode materials for potassium-ion batteries: current status and prospects
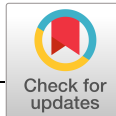
Anode materials for potassium-ion batteries: Current status and prospects

Mo Sha | Long Liu | Huaping Zhao | Yong Lei

Fachgebiet Angewandte Nanophysik, Institut für Physik & IMN MacroNano® (ZIK), Technische Universität Ilmenau, Ilmenau, Germany

Correspondence
Yong Lei, Fachgebiet Angewandte Nanophysik, Institut für Physik & IMN MacroNano® (ZIK), Technische Universität Ilmenau, 98693 Ilmenau, Germany.
Email: yong.lei@tu-ilmenau.de

Abstract

Potassium-ion batteries (KIBs) as one of the most promising alternatives to lithium-ion batteries have been highly valued in recent years. However, progress in KIBs is largely restricted by the sluggish development in anode materials. Therefore, it is imperative to systematically outline and evaluate the recent research advances in the field of anode materials for KIBs toward promoting the development of high-performance anode materials for KIBs. In this review, the recent achievements in anode materials for KIBs are summarized. The electrochemical properties (ie. charge storage mechanism, capacity, rate performance, and cycling stability) of these reported anode materials, as well as their advantages/disadvantages, are discerned and analyzed, enabling high-performance KIBs to meet the requirements for practical applications. Finally, technological developments, scientific challenges, and future research opportunities of anode materials for KIBs are briefly reviewed.

KEYWORDS

anode materials, capacity and stability, electrochemical properties, energy density, potassium-ion batteries

1 | INTRODUCTION

Due to the depletion of fossil fuels and the environmental pollution, clean and renewable energies such as solar, wind, tide, and geothermal play an important role in realizing the sustainable development of human society, and thus have become the fastest-growing renewable energy resources.[1-16] However, these clean energies are always inherently intermittent, resulting in a conflict between energy harvesting and consumption from the aspects of time and space.[15,17-22] To this end, the energy storage system (ESS) is considered to be an effective solution to store and deliver these intermittent energies.[23] So far, lithium-ion batteries (LIBs) are the dominant ESS technology and have become indispensable in our daily life attributed to their convenience, high energy densities and lack-of-memory property.[24-27] With the rapid expansion of LIB applications, LIBs can hardly satisfy the growing demand for the future ESS, because of the relative scarcity (0.0017 wt% in the Earth's crust) and uneven distribution of lithium source.[28]

As a potential alternative to LIBs, sodium-ion batteries (SIBs) have attracted much attention owing to their high abundance of sodium in the Earth's crust and the low cost (Figure 1A).[29-31] Nevertheless, the relatively high-standard redox potential of Na/Na$^+$ (-2.71 V vs the standard hydrogen electrode [SHE], as shown in Table 1) leads to the smaller energy density of SIBs than that of
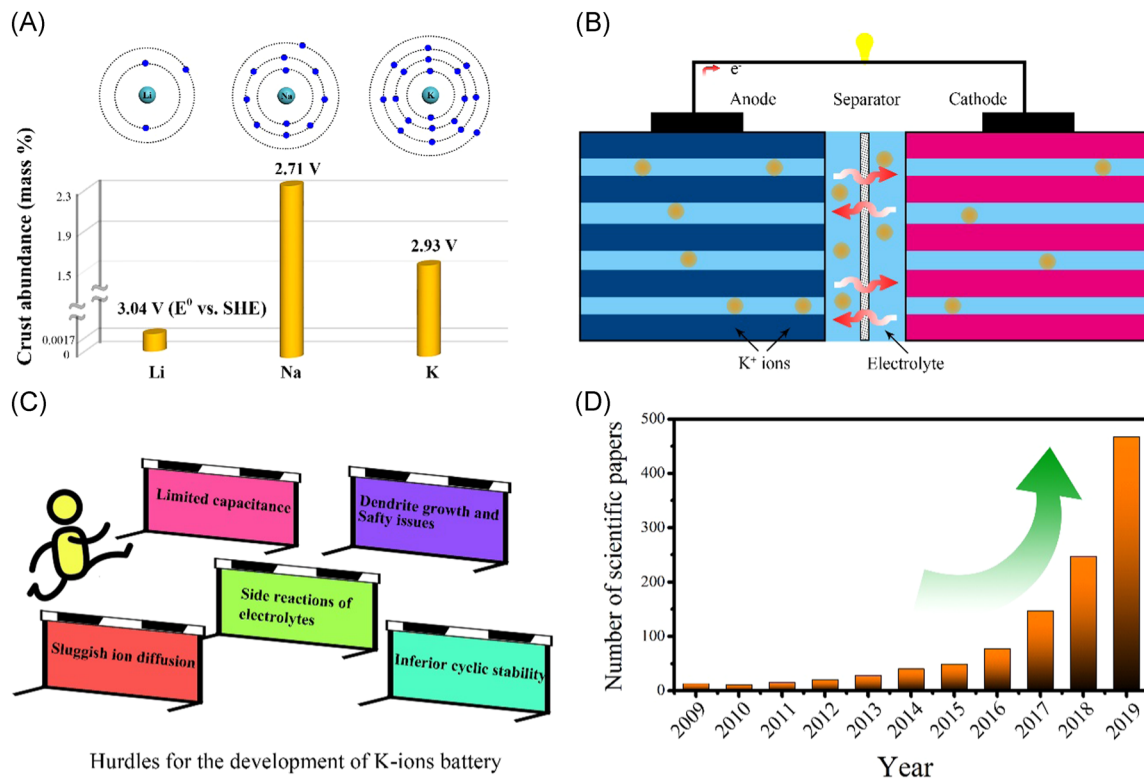
FIGURE 1 A, Abundance of Li, Na, and K metals in the Earth's crust (wt%). B, Schematic illustration of potassium-ion batteries (KIBs). C, Summary of challenges and their relationships to the KIBs. D, Number of publications on KIBs according to Web of Science

LIBs, and thus render their applications in portable electronics and electric vehicles.[32-34] Like lithium and sodium, potassium has similar chemical properties, which means that potassium can be utilized as the potential charge carrier and correspondingly the potassium-ion batteries (KIBs) could operate with similar principles as LIBs and SIBs. In KIBs, K^+ ions shuttle between the cathode and the anode via a K^+-rich electrolyte during the charge/discharge process, which is also termed as "rocking-chair" batteries like LIBs (Figure 1B). In comparison to LIBs and SIBs, KIBs exert three significant advantages of potassium.[34-39] First, the lower standard redox potential of K/K^+ (-2.93 V vs SHE) which is much closer to that of Li/Li^+(-3.04 V vs SHE) enables KIBs to have a potentially higher energy density than SIBs.[40] Second, the abundance of potassium in the Earth's crust would result in a lower cost of KIBs.[41] Third, the weaker Lewis acidity and the corresponding smaller Stokes' radius of K^+ than those of both Li^+ and Na^+ could lead to the highest conductivity and ion mobility of K^+ in the electrolyte.[42,43]

However, it should be admitted that the current development of KIBs is still facing four significant challenges (Figure 1C). First, KIB electrodes with high capacity to guarantee high energy density are still lacking. Second, the rate performance of KIBs is restricted by

the relatively low diffusivity of large K^+ ions in solid electrodes.[43] Third, the low electrochemical potential of K^+/K leads to more side reactions because the solvent in the electrolyte is more easily reduced on the surface of the electrode.[44] Finally, also plagued by the large K^+ ions, the electrode materials of KIBs usually suffer from pulverization-induced capacity fading arising from a large volume expansion during the potassiation/depotassiation process.[45] To address these challenges, much research efforts are devoted to understanding the electrochemical mechanism to effectively solve these problems and significantly improve the energy-storage performance of KIBs (Table 2).

So far, an astounding, increasing number of publications have reported on KIBs (Figure 1D),[36,85] and most research is focused on the development of high-performance electrode materials, both cathodes and anodes. Particularly for anode materials that are carriers of K^+ and electrons in the charging process, volume expansion and structural damage along with the de/intercalation of K^+ ions are unavoidable issues due to the large radius of K^+ ion, and thus, anode materials play a significant role in the energy density and long stable cyclability of KIBs. In this review, recent research progress on anode materials for KIBs is outlined, with respect to the design and development of novel anode materials,

TABLE 1 Physical/electrochemical properties and economic parameters of lithium, sodium, and potassium

Physical/electrochemical properties/economic parameters	Li	Na	K
Atomic number	3	11	9
Atomic mass, u	6.941	22.989	39.098
Density, g cm^{-3}	0.535	0.968	0.856
Melting point, °C	180.45	97.72	63.38
Atomic radius, pm	145	180	220
Ionic radius, Å	0.76	1.02	1.38
Covalent radius, pm	128	166	203
Electronic shell structure	(1, 2)	(1, 2, 8)	(1, 2, 8)
Electronic configuration	(He) 2s^1	(Ne) 3s^1	(Ar) 4s^1
Voltage vs SHE, V	−3.04	−2.71	−2.93
Theoretical capacity of the metal electrode, mAh g^{-1}	3861	1166	685
Crust abundance, mass %	0.0017	2.3	1.5
Crust abundance, molar %	0.005	2.1	0.78
Cost of carbonate, US\$ ton^{-1}	6500	200	1000
Cost of industrial-grade metal, US\$ ton^{-1}	100 000	3000	13 000

particularly for the studies which show an obvious effect on the capacity and stability improvement of KIBs. A unique insight into the existing challenges and future directions of anode materials for KIBs is given in Section 3.

2 | CARBON-BASED MATERIALS

Owing to the remarkable K$^+$ de/intercalation ability, graphite has been first studied as an anode for KIBs. As the research developed, many novel carbon-based anode materials, besides graphite, have been explored in the last few years, such as soft carbon, hard carbon (HC), and nongraphite nanostructured carbon.

2.1 | Graphite materials

Since the 1940s, K-graphite intercalated compounds (K-GICs) have been reported.[86-88] These compounds were synthesized by using a two-zone vapor transport route, in which K vapor is introduced in a custom-made double furnace with graphite. In this method, several kinds of K-GIC are found to be formed at different stages during

the synthesis process, including KC$_8$ in Stage I, KC$_{24}$ in Stage II, KC$_{36}$ in Stage III, and KC$_{48}$ in Stage IV.[89] Nishitani et al[90,91] found K atoms distributed irregularly on the hexagonal carbon centers of adjacent graphite layers. Similar to the case of Li-GICs, the different stages of K-GICs were proved, according to the number of graphene layers being separated into the K-intercalated layer. For instance, K-GICs (KC$_8$) in stage featured one graphene layer for every K-intercalated layer, which means all the graphene layers were intercalated.

A density functional theory (DFT) study about the intercalation behavior of alkali metals (Li, Na, and K) in graphite reveals that the formation enthalpy of KC$_8$ (−27.5 kJ mol^{-1}) is much lower than that of LiC$_6$ (−16.5 kJ mol^{-1}), which suggests that K$^+$ ions can more easily intercalate in graphite.[89] Moreover, DFT calculations also indicate that KC$_8$ has the largest diffusion coefficient, which again highlights the advantage of K$^+$ ion intercalation in graphite.[92] Furthermore, the kinetics during the formation of K-GICs were investigated through DFT calculation with the dispersion correction method, and the results demonstrate that the migration of K$^+$ ions via the vacancy mechanism rather than the Frenkel mechanism.[93] The K-storage mechanism in graphite was further experimentally verified by assembling and characterizing K/graphite cells.

Jian et al[46] first took the lead in finding the experimental K-storage properties of graphite. Here, graphite is the working electrode, K metal is the counter electrode, and 0.8 M KPF$_6$ in 50:50 ethylene carbonate (EC):diethyl carbonate (DEC) is the electrolyte. The resultant K/graphite cell exhibited a high specific discharge capacity of 273 mAh g^{-1} at C/40 rate, which is close to the theoretical capacity of 279 mAh g^{-1} for the formation of KC$_8$ (Figure 2A). Also, because of the solid electrolyte interphase (SEI) film formation, the Coulombic efficiency (CE) can stabilize well at ~99%, (Figure 2B). Ex-situ X-ray diffraction (XRD) measurements of electrochemically discharged anode materials reveal that stage-1 KC$_8$ forms via stage-3 KC$_{36}$ and stage-2 KC$_{24}$ as intermediate phases where the phase transformations are reversible in converting the KC$_8$ back to the less-crystalline graphite (Figures 2C,D). However, stage-4 and -5 compounds were hard to observe during the electrochemical process. Meanwhile, a large volume expansion ~61% is observed upon potassiation, which leads to the fast capacity fading and mediocre rate capability of the graphite anode.

Optimizing binders and electrolytes are an efficient solution to tackle the inferior cycling and rate capabilities of graphite anode.[47,49] For example, replacing polyvinylidene difluoride with sodium polyacrylate (PANa) can drastically improve the first-cycle CE, cyclic stability, and rate capability due to the preformed-SEI effect of the

TABLE 2 Summary of recent anode materials for potassium-ion batteries

Material	Reaction	Voltage (V)	Initial capacity (mAh g^{-1})	Initial Coulombic efficiency	Best capacity retention	Best rate performance	Reference
Graphite	Insertion	0.01-1.5	273	57.4%	81.4% at 2 C	30.4% at 5 C	46
Graphite	Insertion	0.01-1.5	279	87%	98% at 25 mA g^{-1}	≈95% at 15 C	47
Graphite	Insertion	0.01-1.5	246	66.5%	~89% at 20 mA g^{-1}	~20% at 200 mA g^{-1}	48
Graphite	Insertion	0.01-2.0	~100	~78.9%	91% at 10 mA g^{-1}	~77% at 3C	49
Polynanocrystalline graphite	Insertion	0.01-2.0	224	54.10%	50% at 240 mA g^{-1}	44.8% at 200 mA g^{-1}	50
Expanded graphite	Insertion	0.01-3.0	267	81.56%	105.07%	66.5% at 500 mA g^{-1}	51
Hard carbon/carbon black	Insertion	0.1-1.0	200	~50%	97% at 0.1 C	~27% at 10 C	52
Hard-soft composite carbon	Insertion	0.01-2.0	261	67%	93% at 1 C	35% at 10 C	53
Hard carbon microspheres	Insertion	0.01-1.5	~270	~62%	83% at 0.1 C	52% at 5 C	54
Activated carbon	Insertion	0.01-2.0	~260	~62%	62% at 0.2 A g^{-1}	54% at 1.0 A g^{-1}	55
Few-layer F-doped graphene	Insertion	0.01-2.4	330	41.2%	~50% at 500 mA g^{-1}	65% at 500 mA g^{-1}	56
Nitrogen-doped graphene	Insertion	0.01-1.5	330	80%	96.5% at 100 mA g^{-1}	~14% at 200 mA g^{-1}	57
N-doped carbon microsphere	Insertion	0.01-3.0	240	75%	75% at 1.8 C	62% at 72 C	58
N-doped hierarchically porous carbon	Insertion	0.001-3.0	303	95%	44.4% at 500 mA g^{-1}	67% at 500 mA g^{-1}	59
Phosphorus and oxygen dual-doped graphene	Insertion	0.01-3.0	566.6	22.6%	~95% at 2 A g^{-1}	41% at 2 A g^{-1}	60
Nitrogen- and oxygen-doped carbon nanofiber	Insertion	0.005-3	280	31%	99.5% at 1 C	31% at 10 C	61
Hard carbon–derived from tire rubber	Insertion	0-1.8	181	33%	78% at 0.5 C	~24% at 2 C	62
Porous carbon nanofiber paper	Insertion	0-3.0	272	24.1%	77% at 0.02 A g^{-1}	~25% at 7.7 A g^{-1}	63
Polycrystalline soft carbon	Insertion	0.01-1.5	599		80%		64
Natural nitrogen-doped carbon nanofibers	Insertion	0.01-2.0	215.2	37.80%	90%	35.2% at 1395 mA g^{-1}	65
Nitrogen/oxygen dual-doped hard carbon	Insertion	0.001-3.0	315	25%	76.10%	33% at 3000 mA g^{-1}	66
K$_2$Ti$_4$O$_9$	Insertion	0.01-2.5	97	20%	82% at 0.2 C	20% at 15 C	67
K$_2$Ti$_4$O$_9$	Insertion	0.01-3.0	151	26%	61% at 50 mA g^{-1}	54% at 300 mA g^{-1}	68

(Continues)

TABLE 2 (Continued)

Material	Reaction	Voltage (V)	Initial capacity (mAh g^{-1})	Initial Coulombic efficiency	Best capacity retention	Best rate performance	Reference
K$_2$Ti$_8$O$_{17}$	Insertion	0.01–3.0	118.7	65.4%	93% at 20 mA g^{-1}	37% at 500 mA g^{-1}	69
KTi$_2$(PO$_4$)$_3$/C	Insertion	1.2–2.8	75.6	75%	110% at 0.5 C	80% at 5 C	70
Ti$_3$C$_2$	Insertion	0.01–3.0	136	27%	44% at 200 mA g^{-1}	42% at 300 mA g^{-1}	71
Ti$_3$CNTz	Insertion	0.01–3.0	710	28.40%	10.50%		72
TiSe$_2$	Insertion	1.0–3.0	92.7	~67.1%	69.80%	50% at 1000 mA g^{-1}	73
MoS$_2$	Insertion	0.5–2.0	98	74.4%	97.50%	77% at 2.86 C	74
MoS$_2$@RGO	Insertion/ conversion	0.01–3.0	679	~30%	~100% at 100 mA g^{-1}	26.2% at 0.5 A g^{-1}	75
Co$_3$O$_4$–Fe$_2$O$_3$/C	Conversion	0.01–3.0	~420	54%	~52% at 50 mA g^{-1}		76
CoS@graphene	Insertion	0.01–2.9	434.5	64.4%	70.2% at 0.5 C	56.2% at 4 C	77
SnS$_2$-coated RGO	Conversion/ alloying	0.01–2.0	355	56%	~71.4% at 25 mA g^{-1}	~33.8% at 2 A g^{-1}	78
Sb$_2$S$_3$-S, N-co-doped graphene composite	Conversion	0.1–3.0	548	69.7%	89.4% at 50 mA g^{-1}	~62% at 1 A g^{-1}	79
VSe$_2$		0.01–2.6	366	69.10%	95.10%	45.9% at 2 A g^{-1}	80
Black phosphorus/C	Alloying	0.01–2.0	433.2	58.50%	61%	~63% at 2 A g^{-1}	81
Sn$_4$P$_3$/C	Alloying	0.01–2.0	350	60%	80%	55.6% at 1 A g^{-1}	45
3D carbon network confined Sb nanoparticles	Alloying	0.01–2.0	478	68.20%	96.40%	~60.2% at 1 A g^{-1}	82
K$_2$TP		0.1–2	270	46%	71.8% at 0.2 C	20.3% at 2 C	83
K$_2$PC		0.1–2.0	245	44%	~88% at 0.2 C	32.2% at 2 C	83
K$_2$TP		0.1–2.0	305.8	76.1%		~71% at 1 A g^{-1}	84
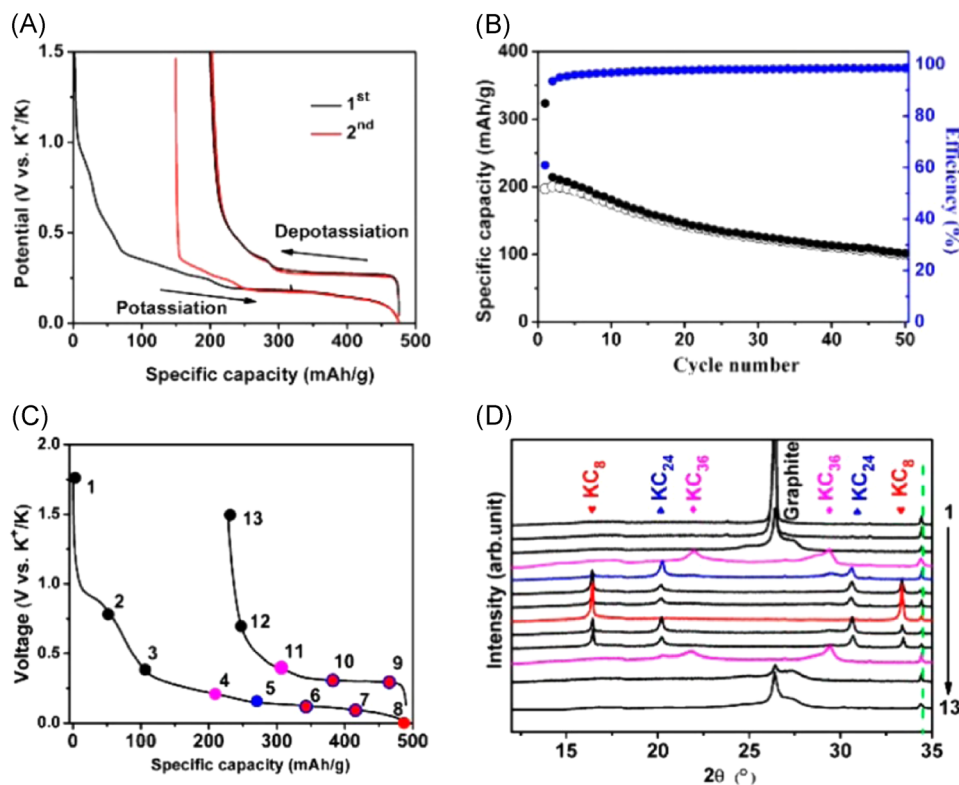
FIGURE 2 A, GPD profiles of graphite for the initial two cycles between 0.01 and 1.5 V at C/40. B, Cycling performance of graphite at C/2. C, First-cycle GPD potential profiles at C/10. D, X-ray diffraction patterns of electrodes corresponding to the marked selected states of charges in (C). Reprinted with permission.[46] Copyright 2015, American Chemical Society

binder PANa. With PANa as the binders, less K is consumed for the formation of SEI-layer in the first discharge cycle of the cell. As the electrolytes also have a strong impact on the formation of stable SEI layers, further tuning the compositions of electrolytes, especially solvents, can also help to improve the performance of the graphite anode. Compared to EC:dimethyl carbonate (EC:DMC) and EC:DEC, EC:propylene carbonate (EC:PC) as the solvent of the electrolytes, enables the graphite anode to have the best capacity retention and the highest first-cycle CE. The reason might be the high solubilizing ability and high ionic conductivity of KPF_6 in EC:PC than those in both EC:DMC and EC:DEC. Apart from graphite, several forms of nongraphite carbon have also been reported to successfully intercalate K, including soft-carbon and hard-carbon microspheres.

2.1.1 | Soft carbon and hard carbon

A kind of soft carbon was synthesized via pyrolysis of 3,4,9,10-perylene-tetracarboxylicacid-dianhydride at 900°C and it delivers a capacity of 273 mAh g^{-1}, which is similar to that of graphite.[53] The problem of soft carbon is that the potential profile of soft carbon-based KIBs exhibits only slopes instead of the plateaus at 0.3 V being observed in

graphite in a graphite/K cell, indicating an unstable discharge voltage. Recently, three kinds of N-doping soft carbon nanofibers (NCNFs) were fabricated by carbonizing polypyrrole nanofibers at 650°C, 950°C, and 1100°C, respectively.[94] These NCNFs have a unique hollow interior structure and rough surface with high structural defects and are beneficial for K-storage (Figure 3A). Besides this, the N-doping content of NCNFs decreases along with the increase of the carbonization temperature (Figures 3B,C). Due to the high N-doping content and unique structure, NCNF-650 shows the best cycling and rate performance among its counterparts. The NCNF-650 exhibits a capacity of 146 mAh g^{-1} at 2 A g^{-1} after 4000 cycles (Figures 3D,E) and a rate capability of 101 mAh g^{-1} at a 20 A g^{-1} (Figure 3F).

Apart from soft carbon, HC can also be used as a KIBs anode with good capacity and long cycle life. More importantly, the discharging plateau of HC is usually above 0.1 V, enabling reducing the risk of K-metal plating and ensure safety. Vaalma et al[95] proved experimentally the electrochemical K$^+$ intercalation behavior of the HC anode based on its initial voltage profile at 0.1 C. This anode outputs capacities of 200 mAh g^{-1} at 0.1 C in the potential window of 0.2 to 2.0 V (Figure 4A). The sloping potential between 1.2 and 0.3 V vs K$^+$/K is mostly associated with the intercalation of K$^+$ ions (100 mAh g^{-1})
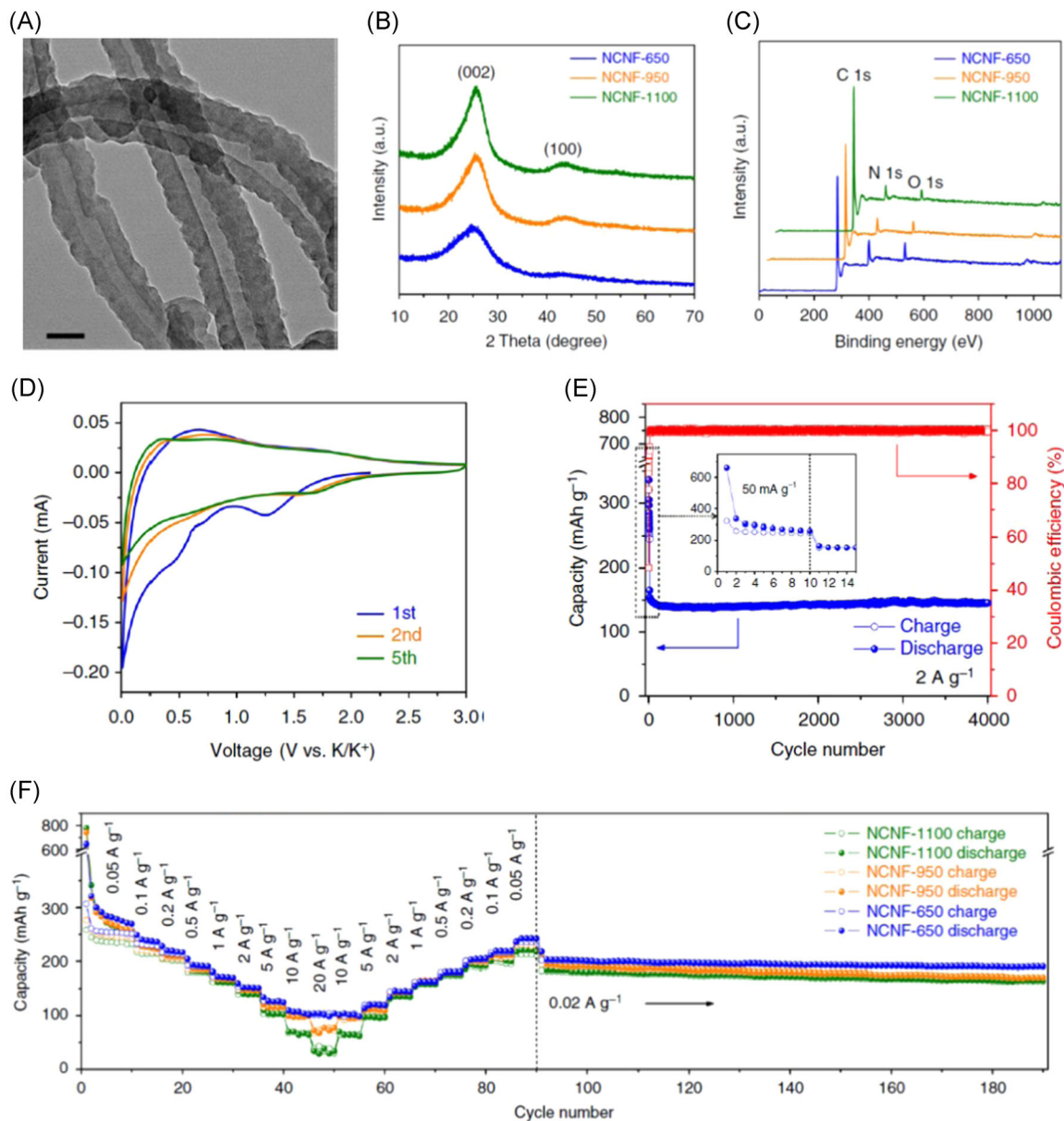
FIGURE 3 A, Transmission electron microscopy image of NCNF-650. (B) XRD patterns and (C) XPS survey spectra of NCNFs. D, CV curves of NCNF-650. E, Long-term cycling performance of NCNF-650 at a high rate of $2\,A\,g^{-1}$. F, Rate performance of NCNFs with rates ranging from 0.05 to $20\,A\,g^{-1}$. Reprinted with permission.[94] Copyright 2018, Springer Nature. NCFC, N-doping soft carbon nanofibers; XPS, X-ray photoelectron spectroscopy; XRD, X-ray diffraction

into the distorted graphitic sheets, while the low-potential plateau between 0.3 and 0.02 V vs K^+/K is correlated with micropore filling ($100\,mAh\,g^{-1}$). Furthermore, the role of high-conductive additives of carbon black (CB) is highlighted, and the rate capacity of the HC/CB electrode is greatly improved by adding CB (Figure 4B).

Doping with heteroatoms, such as nitrogen, sulfur, and phosphorus can effectively increase the capacity of HC materials through generating defect sites and functional groups.[96] A sulfur/nitrogen dual-doped hard-carbon material (SNHC) was prepared via a facile pyrolysis method. The SNHC exhibits abundant defect sites, functional groups, and a hierarchical micro/mesopore structure, which is beneficial to improving the specific capacity. As a result, this SNHC delivers a high capacity of $293.8\,mAh\,g^{-1}$ at $0.1\,A\,g^{-1}$. Furthermore, the cycle performance is highly stable at both low and high rates, with a capacity of $213.7\,mAh\,g^{-1}$ over 500 cycles at $0.1\,A\,g^{-1}$, and $143.6\,mAh\,g^{-1}$ over 1200 cycles at $3\,A\,g^{-1}$, respectively.[97] In addition, a kind of S/O co-doped porous HC microsphere (PCMs) was prepared. The PCMs possess an enlarged interlayer spacing, high surface area, enormous structural defects and functional groups, resulting from the porous framework and the S/O co-doping. Consequently, PCMs exhibit a high capacity of $226.6\,mAh\,g^{-1}$ at
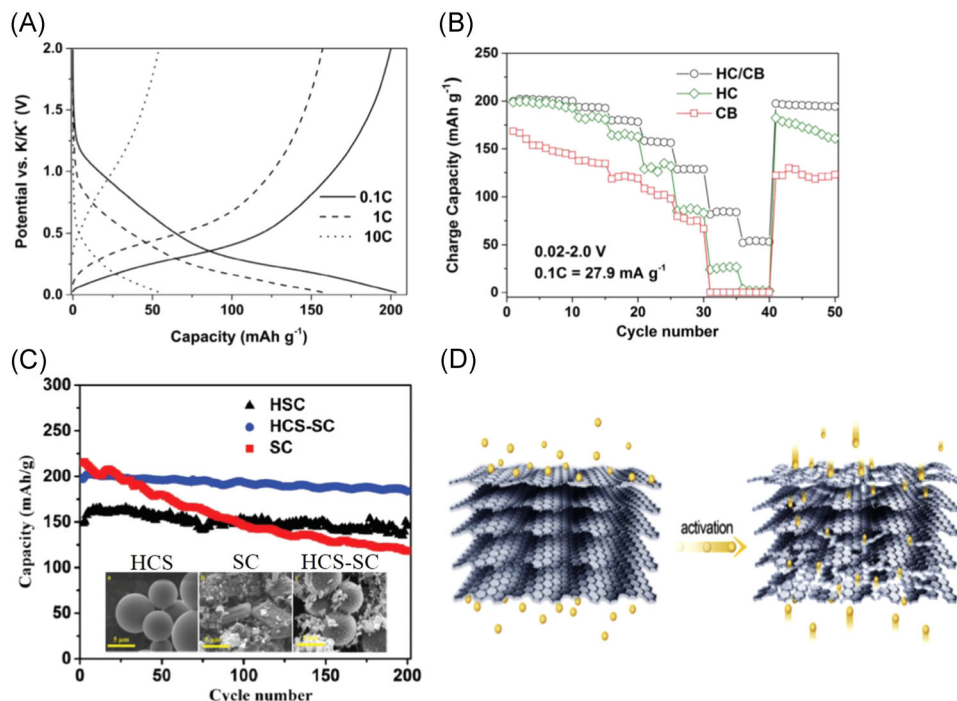
FIGURE 4 A, Potential profiles recorded at 0.1 C (cycle 10), 1 C (cycle 28), and 10 C (cycle 38) for the HC/CB composite. B, Rate Performance of HC, CB, and HC/CB within 0.02 and 2.0 V range. Reprinted with permission.[95] Copyright 2016, ECS. D Long cycling performance at 1 C rate of hard carbon spheres (HCS), SC, and HCS-SC. Reprinted with permission.[53] Copyright 2017, John Wiley and Sons; D, Schematic illustration of the activation process. Reprinted with permission.[55] Copyright 2017, Elsevier. CB, carbon black, HC, hard carbon; SC, soft carbon

50 mA g^{-1} after 100 cycles and superior rate capability of 158.1 mAh g^{-1} at 1000 mA g^{-1}. Furthermore, it can also maintain a highly reversible capacity of above 108.4 mAh g^{-1} for over 2000 cycles at 1000 mA g^{-1}.[98]

A hard-soft carbon composite was recently designed to improve the limited rate capability of HC and the capacity fading of SC.[54] Compared with the pure SC and HC, the hard-soft carbon composite, with 20 wt% SC distributed in a matrix-phase of HC microspheres, exhibits a high specific capacity and rate performance. It displays a superior initial capacity of 261 mAh g^{-1} at 0.1 C and outstanding cycle performance of 93% capacity retention after 200 cycles at 1 C (Figure 4C). As another nongraphite carbon, activated carbon shows a similar intercalation behavior as graphite. This activated carbon exhibits relatively large d-spacings in the (100) crystal planes (graphite: 0.334 nm vs activated carbon: 0.358 nm), being beneficial to facilitating rapid intercalation/deintercalation of K$^+$ ions (Figure 4D).

2.1.2 | Nanostructured nongraphite carbon

Nanostructured carbon materials, such as carbon nanofibers (CNFs) and graphene, can also be utilized as anodes for KIBs. Self-supported free-standing CNFs arrays can directly serve as electrodes without binders.[31] The CNFs display a high initial discharge capacity of 680 mAh g^{-1} at 50 mA g^{-1} in the first cycle and gradually stabilizes at 80 mAh g^{-1} after 20th cycles.[99] Similarly, porous CNFs with a high rate capacity of 100 mAh g^{-1} at 7.7 A g^{-1} were reported (Figure 5A).[63] Moreover, a negligible capacity decay per cycle was observed with the capacity changing from 270 to 211 mAh g^{-1} after 1200 cycles at 20 mA g^{-1}, ascribed to the fact that the porous structure can effectively relieve the volume expansion during the intercalation of K$^+$ ions.

Graphene has also been investigated as a potential anode for KIBs.[101] Reduced graphene oxide fabricated from a modified Hummer's method delivers a capacity of about 50 mAh g^{-1} at 100 mA g^{-1} which is much smaller than that of graphite.[102] Share et al[100] used few-layer graphene (FLG) as anode and investigated its electrochemical performance. The FLG produced reversible capacities of ~150 mAh g^{-1} at 100 mA g^{-1} for 100 cycles, with CEs over 90%. The intercalation mechanism of K$^+$ ions into FLG was revealed via in situ Raman spectroscopy, which enables comparing the ratio of the graphene uncharged peak and charged peak in the Raman spectra and assigned them to the different stages of K-GICs (Figures 5B,C). A one-/two-dimensional
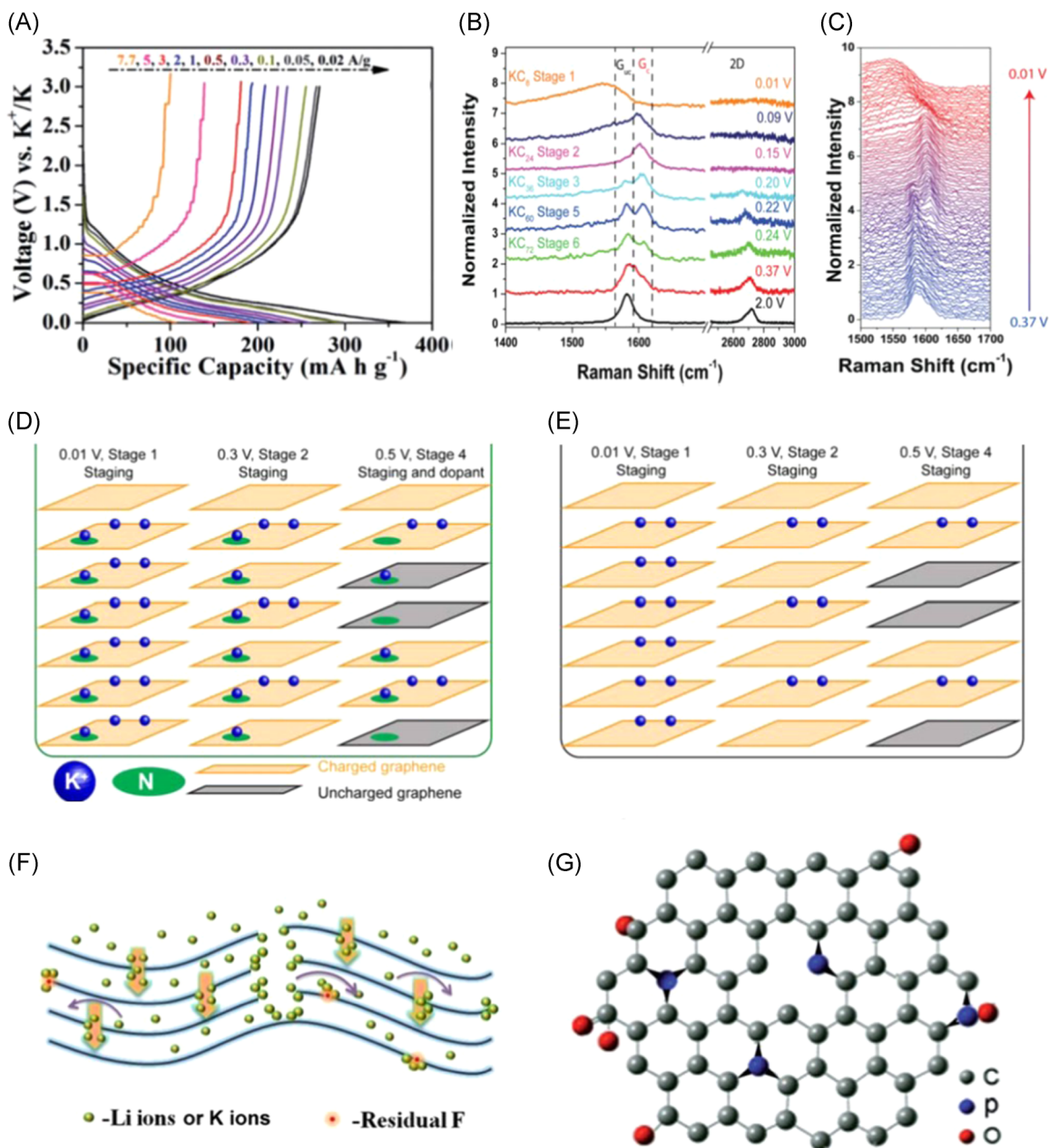
FIGURE 5 A, Voltage profiles of the carbon nanofiber anodes in potassium-ion batteries. Reprinted with permission.[63] Copyright 2017, The Royal Society of Chemistry. B, Selective Raman spectra taken at different states of charge as indicated in the LSV. C, Waterfall plot of all Raman spectra taken between 0.37 and 0.01 V. Reprinted with permission.[100] Copyright 2016, The Royal Society of Chemistry. D, Schematic of the staging and defect storage mechanism in N-FLG and FLG (E). Reprinted with permission.[57] Copyright 2016, American Chemical Society. F, Li, or K-ion diffusion mechanism. Reprinted with permission.[56] Copyright 2016, American Chemical Society. G, Schematic of phosphorus and oxygen dual-doped graphene. Reprinted with permission.[60] Copyright 2017, The Royal Society of Chemistry. FLG, few-layer graphene

(1D/2D) C_3N_4/rGO composite was synthesized and the unique 1D/2D morphology prevents the restacking of graphene layers and aggregation of C_3N_4 nanoparticles. Owing to this unique structure, the composite delivers a specific capacity of 464.9 mAh g^{-1} after 200 cycles at 1 A g^{-1}. Furthermore, it showed minimal capacity fading with 228.6 mAh g^{-1} after 1000 cycles at 10 A g^{-1}.[103]

Noteworthily, heteroatom (F, N, P, B, and O) doping into the carbon matrix tends to create defect sites that can attract alkali ions, and meanwhile, improve the electrical conductivity properties of a carbonaceous matrix by enhancing the ion/electron diffusion velocity.[104-109] The nitrogen doping of FLG can increase the K$^+$ ion storage capability to over 350 mAh g^{-1}, demonstrating N-doping activates the

distributed storage sites in the carbon lattice and, therefore, offers extra charge capacity (Figures 5D,E).[57] Recently, a few-layer F-doped graphene foam was prepared, exhibiting a high capacity of 165.9 mAh g^{-1} at 500 mA g^{-1} after 200 cycles.[56] The high electrochemical performance is largely ascribed to the improvement of the electrochemical reactivity and numerous defect sites, as well as electrical conductivity, attributed to F-doping and the unique framework (Figure 5F). Dual-doped graphene (PODG) material with P and O doping is another example.[60] The large interlayer spacing induced by P and O dual doping enables the PODG to deliver a high capacity of 474 mAh g^{-1} at 50 mA g^{-1} after 50 cycles and it retained a capacity of 160 mAh g^{-1} at 2000 mA g^{-1} after 600 cycles. (Figure 5G).

2.2 | Noncarbon-based materials

Noncarbon-based anodes are another important anode candidate for KIBs. According to the K$^+$ ions storage mechanism, the noncarbon anodes are generally divided into three main categories, that is, intercalation compounds, alloying compounds, and conversion-type compounds.

2.2.1 | Noncarbon-based intercalation anodes

For secondary batteries, titanium-based materials are one of the important intercalation anodes. Among them, Li$_4$Ti$_5$O$_{12}$ and Na$_2$Ti$_3$O$_7$ have been widely studied as intercalation anodes for LIBs and SIBs. Analogs of these compounds like potassium tetratitanate (K$_2$Ti$_4$O$_9$) are believed to be promising intercalation anodes for KIBs.

K$_2$Ti$_4$O$_9$ has a layered structure with an interlayer gap suitable for accommodating K ions (Figure 6A).[67] It exhibits an initial discharge capacity of 80 mAh g^{-1} at 100 mA g^{-1} and 97 mAh g^{-1} at 30 mA g^{-1}, respectively. To improve the cyclic stability of K$_2$Ti$_4$O$_9$, further modifications such as control of particle size and porosity is carried out. For instance, ultrathin nanoribbons of potassium titanate (M-KTO, K$_2$Ti$_4$O$_9$) were fabricated by simultaneous oxidation and alkalization process of Ti$_3$C$_2$ MXene nanosheets (Figure 6B).[68] M-KTO has suitable interlayer spacing, ultrathin thickness, and narrow width as well as an open microporous network. As a result, it exhibits an outstanding reversible capacity of 151 mAh g^{-1} at 50 mA g^{-1} and long-term stable cyclability over 900 cycles.

As another titanium-based compound, unique K$_2$Ti$_8$O$_{17}$ nanorods were prepared and studied as anodes for KIBs.[69] The special nanorod morphology of K$_2$Ti$_8$O$_{17}$ provides both a large contact area with the electrolyte and numerous surface-active sites, beneficial for K$^+$ ions storage (Figures 6C,D).

Furthermore, the stepped layered structure of TiO$_6$ octahedrons has large interstitial spaces and open channels for K$^+$ ions fast transport. Benefiting from the unique structure, K$_2$Ti$_8$O$_{17}$ nanorods have a high initial discharge capacity of 181.5 mAh g^{-1} at 20 mA g^{-1} and retain 110.7 mAh g^{-1} after 50 cycles, as well as a high rate capacity of 44.2 mAh g^{-1} at 500 mA g^{-1}.

KTi$_2$(PO$_4$)$_3$ is a kind of NASICON-type polyanionic compound, its structure has enough space to accommodate K$^+$ ions transport into the crystal, which benefits the cycling stability of KIBs, as shown in Figures 6E,F.[111] Although the three-dimensional (3D) framework of the KTi$_2$(PO$_4$)$_3$ crystal provides large interstitial spaces and offers open channels for K-ion transport, their conductivity is relatively low. In response to this issue, a nanocubic KTi$_2$(PO$_4$)$_3$ was prepared and coated with a thin layer of carbon to improve its electronic conductivity. The carbon-coated KTi$_2$(PO$_4$)$_3$ delivers a discharge capacity of 75.6 mAh g^{-1} at 0.5 C in the first cycle and retains cycling stability up to 100 cycles.

Recently, 2D transition metal carbides and carbonitride (MXene) materials have attracted much attention because of their intriguing geometry and electronic and electrochemical properties. Usually, MXenes are synthesized by etching thin metal layers from MAX phases, where M stands for the transition metal (eg. Ti, V, Cr, Mo, and Nb), A represents the elements from groups 13 and 14 (eg. Al, Si, Sn, and Ga), X signifies carbon and/or nitrogen.[112-115] A Ti$_3$CNT$_z$ anode was developed by etching aluminum from their corresponding MAX phases.[116] It shows an ultrahigh initial discharge capacity of 710 mAh g^{-1} at 20 mA g^{-1} but poor cycling stability, only 75 mAh g^{-1} capacity was maintained after 100 consecutive cycles. The XRD study indicates that there is an irreversible expansion in the c-lattice of this Ti$_3$CNT$_z$ at the first potassiation cycle because K$^+$ ions were trapped and blocked between the layers and hardly extracted at the following cycles and, thus, lead to significant capacity fading (Figure 7A). To improve the electrochemical performance, alkalized Ti$_3$C$_2$ MXene nanoribbons were fabricated with a unique structure.[72] Benefiting from the expanded interlayer spacing, 3D porous framework, and narrow widths, Ti$_3$C$_2$ delivers a high reversible capacity of 136 mAh g^{-1} at 20 mA g^{-1} and an outstanding long-term cyclability of about 42 mAh g^{-1} after 500 cycles at 200 mA g^{-1}.

MoS$_2$ has an S-Mo-S layered structure and is able to maintain a wider interlayer spacing and an open 2D diffusion pathway for K$^+$ ion intercalation and transportation.[117] Owing to the stable layered structure, MoS$_2$ shows good cycle stability with 97.5% of the 10th capacity retained after 200 cycles at 20 mA g^{-1}.[74] Furthermore, the K$^+$ ion intercalation process and the corresponding phase
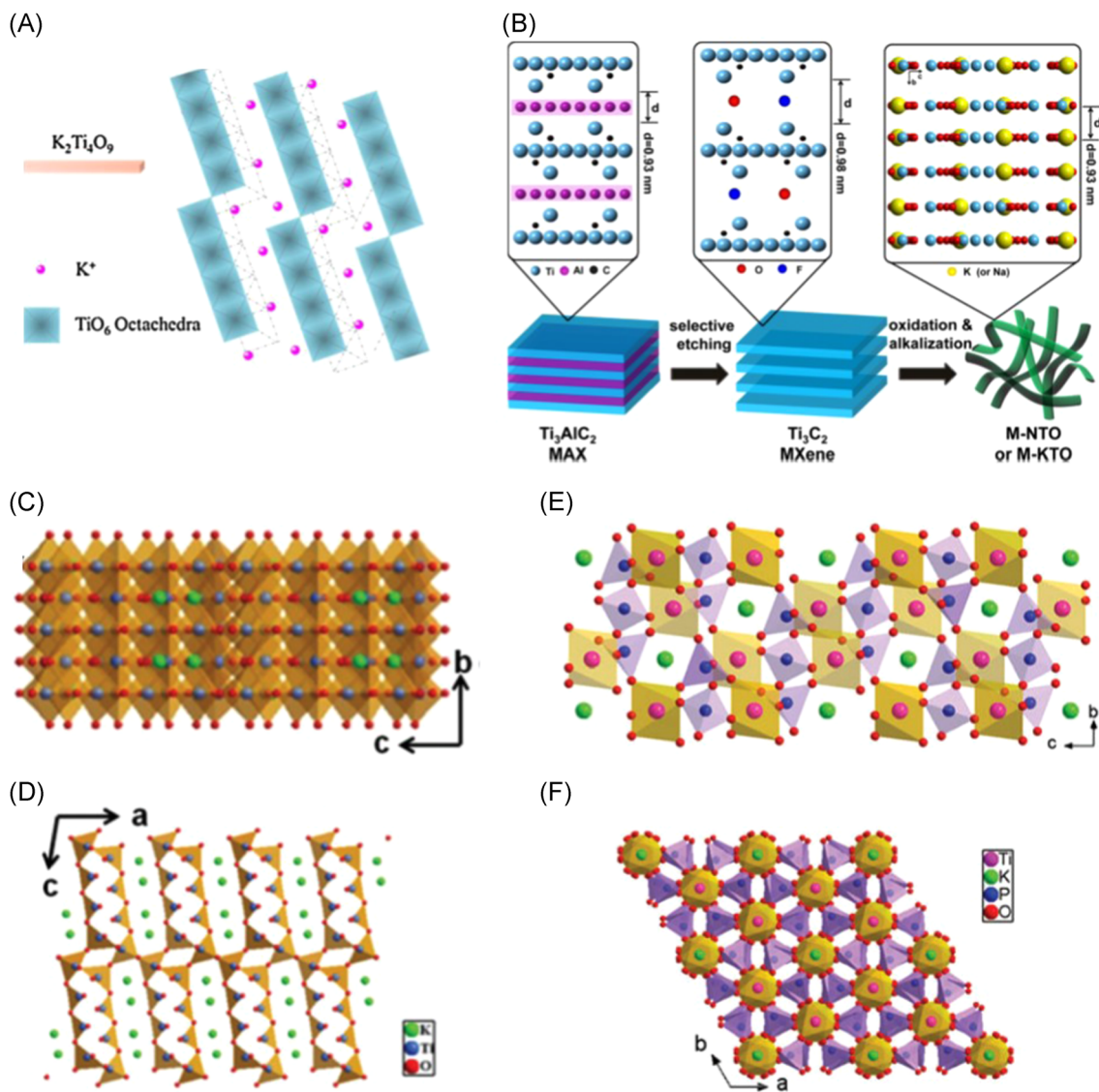
FIGURE 6 A, Crystal structure of $K_2Ti_4O_9$. Reprinted with permission from Yang Cao et al[110] Copyright 2014, Elsevier. B, Schematic illustration of the fabrication of M-NTO (nanoribbons of sodium titanate, $NaTi_{1.5}O_{8.3}$) or M-KTO nanoribbons. Reprinted with permission.[68] Copyright 2017, American Chemical Society; C, D, Projections of the $K_2Ti_8O_{17}$ structure along the[79] [100] and [010] directions. Reprinted with permission.[69] Copyright 2016, The Royal Society of Chemistry; E, F, Projections of the $KTi_2(PO_4)_3$ structure along the[79] [100] and [001] directions respectively. Reprinted with permission.[111] Copyright 2016, the Royal Society of Chemistry. KTO, potassium titanate

evolutions in MoS_2 were also revealed. In detail, a hexagonal K_xMoS_2 ($x > 0.4$) was formed in the process of intercalation and the phase is unstable when reaching a higher K^+ ion intercalation ratio, leading to the degradation of MoS_2 and reduction to Mo and K_xS species. To further improve the electrochemical performance, petal-like MoS_2 nanosheets vertically grown on graphene sheets (MoS_2@rGO) were fabricated via a two-step solvothermal method (Figure 7B).[75] Owing to the synergistic effect of MoS_2 nanosheets and the flexible graphene backbone, the composites deliver a high initial charge capacity of 679 mAh g^{-1} at 20 mA g^{-1} and retain a charge capacity of 380 mAh g^{-1} at a 100 mA g^{-1} after 100 cycles. Compared to the MoS_2 and rGO counterparts,

MoS_2@rGO shows the best rate performance with capacities of 427, 313, 232, and 178 mAh g^{-1} at 50, 100, 200, and 500 mA g^{-1}, respectively (Figure 7C).

The large interlayer space and high electrical conductivity also make metal selenide materials (such as $MoSe_2$ and $TiSe_2$) attractive for KIBs. A carbon-coating and N-doping $MoSe_2$ composite shows a good rate performance and long cycling stability with a discharge capacity of 258 mAh g^{-1} at 100 mAh g^{-1} after 300 cycles and a capacity of 197 mAh g^{-1} at 1000 mA g^{-1}.[118] $TiSe_2$ was synthesized via a powder-sintering approach and the crystal structure is shown in Figure 7D.[73] Owing to the large interlayer space, $TiSe_2$ delivers an initial charge capacity of 92.7 mAh g^{-1} and maintains a reversible
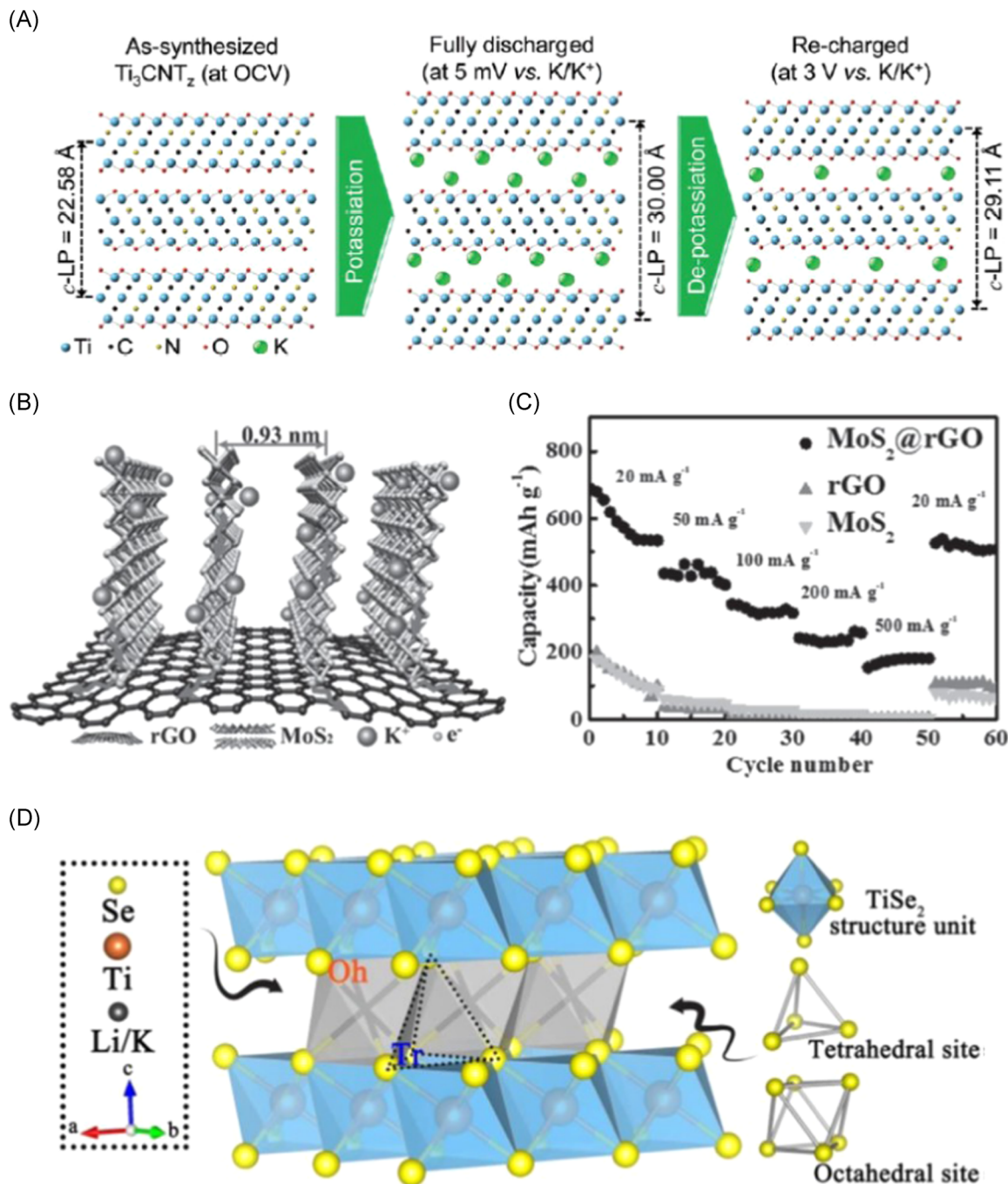
FIGURE 7 A, Schematic for the structure of Ti_3CNO_2 before and after electrochemical potassiation and depotassiation. O_2 was used instead of T_z for simplicity (c-LP stands for the c-lattice parameter). Reprinted with permission.[72] Copyright 2017, The Royal Society of Chemistry. B, Schematic illustration showing the paths for K-ion diffusion and electron conduction in the MoS_2@rGO composites. C, Rate performances of the MoS_2@rGO, MoS_2 particle, and pure rGO anodes at different current densities. Reprinted with permission.[75] Copyright 2017, John Wiley and Sons. D, Crystal structure of $TiSe_2$ with octahedral sites (Oh) as well as the adjacent tetrahedral sites (Tr). Reprinted with permission.[73] Copyright 2018, Elsevier

capacity of 64.7 mAh g^{-1} after the 100th cycle at 65 mA g^{-1}. Furthermore, the potassiation/depotassiation reaction mechanism was unraveled by the analysis of in situ XRD, during the intercalation/extraction process of K$^+$ ions, $TiSe_2$ goes through three-phase stages of $K_{0.25}TiSe_2$, $K_{0.58}TiSe_2$, and K_xTiSe_2 (x ≈ 0.7) by a series of tests.

2.2.2 | Conversion-type anodes

Several transition metal oxides and transition metal sulfides have been reported as conversion anodes, owing to their high theoretical capacities and redox reversibility. A composite of Co_3O_4-Fe_2O_3 nanoparticles in a super

P carbon matrix (Co_3O_4-Fe_2O_3/C) was fabricated via the molten salt method, and here, the carbon matrix is able to enhance the conductivity as well as reduce the impact of volume change.[76] The electrochemical reaction process in the hybrid Co_3O_4-Fe_2O_3/C was proposed as follows: (a) $Fe_2O_3 + 6K^+ + 6e^- \rightleftharpoons 2Fe + 3K_2O$ and (b) $Co_3O_4 + 8K^+ + 8e^- \rightleftharpoons 3Co + 4K_2O$. This composite delivers a high reversible capacity of 220 mAh g^{-1} at 50 mA g^{-1} for 50 cycles. A Co_3O_4@N-doped composite with a N-doped amorphous carbon layer coating over Co_3O_4 nanoparticles was studied as another example. Due to the conductive carbon layer, the conductivity and K^+ diffusion rate of the composite were increased, and the layer also inhibited the formation of aggregated intermediates, improving the cycling performance. Due to these advantages, the Co_3O_4@N-C was able to retain about 213 mAh g^{-1} after 740 cycles.[119] Likewise, a composite of SnS_2-rGO was designed by treating the peroxostannate-graphene oxide composite with H_2S.[120] The composite exhibits a high initial capacity of about 350 mAh g^{-1} and retains over 250 mAh g^{-1} after 30 cycles. Later on, CoS quantum dot (QDs) nanoclusters anchored on graphene nanosheets (CoS@G-25) were reported (Figure 8A).[77] CoS QDs display a capacity of 310.8 mAh g^{-1} at 500 mA g^{-1} for 100 cycles. Subsequently, an architecture of Sb_2S_3 nanoparticles dispersed in porous S, N co-doped graphene framework (Sb_2S_3-SNG) was designed and shows good electrochemical performance, attributed to the porous co-doping graphene framework, which can buffer volume expansion and promote fast electron and ion transfer.[79] In detail, it exhibits a high reversible capacity of 548 mAh g^{-1} at 20 mA g^{-1}, outstanding cycling stability with a CE of 89.4% at 50 mA g^{-1} for 100 cycles, and an excellent rate capability of 340 mAh g^{-1} at 1000 mA g^{-1}.

Similarly, VSe_2 also follows a combination of intercalation and conversion reactions. It consists of two steps: first, K^+ ions intercalate into VSe_2 to form K_xVSe_2 (Figure 8B) and second, K_xVSe_2 decomposes into V and K_2Se through a conversion reaction.[80] Benefiting from the merits of a unique 2D nanostructure and high electron/ion conductivity, the nanosheets output a high reversible capacity of 366 mAh g^{-1} at 100 mA g^{-1} and a high rate capability of 169 mAh g^{-1} at 2000 mA g^{-1}.

2.2.3 | Alloy anodes

Alloy anodes take advantage of the alloying reactions between certain elements (group 14 or 15 elements) and alkali metals to achieve surprisingly higher specific capacities for KIBs.[122-125] With the help of DFT calculations, the energetics associated with different anode materials were computed, indicating high theoretical

capacities might be achieved by alloy anodes.[126] However, the volume expansion for the K alloying anodes is also large because of the intrinsically larger ionic radius of K^+ ions. As a result, strategies (morphology optimization and surface engineering, etc.) should be found for the alloy anodes to prevent active material pulverization upon cycling and obtain better electrochemical performance.

McCulloch et al[127] first reported the electrochemical model of the Sb-C composite as KIBs anodes and the Sb-C composite exhibits a high reversible capacity of 650 mAh g^{-1}, about 98% of theoretical capacity.[127] Thereafter, a 3D SbNPs@C composite was developed with Sb nanoparticles being wrapped into the 3D carbon framework via a freeze-drying treatment. The unique 3D structure network improves the effective contact area between electrode and electrolyte (Figure 8C).[121] In addition, the carbon matrix can not only avoid the agglomeration of Sb particles but also enhances the conductivity of the overall electrode. The 3D SbNPs@C anode delivers a high reversible capacity of 478 mAh g^{-1} at 200 mA g^{-1} and a remarkable rate capability of 288 mAh g^{-1} at 1000 mA g^{-1}. Furthermore, the reaction mechanism is investigated through in situ XRD analysis, concluding a two-step alloying process where an intermediate phase K_xSb and a K_3Sb phase are formed during the cycles. Recently, a unique Sb@CSN (Sb nanoparticles @ carbon sphere network) composite was prepared and shows a high capacity of 551 mAh g^{-1} at 100 mA g^{-1} after 100 cycles with only a 0.06% capacity decay per cycle and 504 mAh g^{-1} after 220 cycles at a high current density of 200 mA g^{-1}.[128]

An Sn-carbon composite was prepared and showed a reversible capacity of 110 mAh g^{-1} at 25 mA g^{-1} after 30 cycles.[129] Furthermore, in situ XRD tests demonstrated the working principle of Sn anodes with the K_2Sn_5 and K_4Sn_{23} forming in the reaction process. Later, the reaction mechanism of Sn anodes in KIBs was further revealed using in situ TEM testing by Wang et al.[130] A two-step potassiation mechanism was proposed: (1) the formation of a KSn phase after full reaction and (2) the reversible formation of the nanopore and pulverization during the cycling of Sn nanoparticles.

A Sn_4P_3/C electrode was prepared with a good cycling capacity of 307.2 mAh g^{-1} after 50 cycles and a good rate capability of 221.9 mAh g^{-1} at 1 A g^{-1}.[45] The mechanism of this composite may be described as follows: (a) $Sn_4P_3 + (9-3\times)K \rightleftharpoons 4Sn + 3K_{3-x}P$, (b) $23Sn + 4K \rightleftharpoons K_4Sn_{23}$, and (c) $K_4Sn_{23} + 19K \rightleftharpoons 23KSn$. Upon potassiation, a conversion reaction first occurs where the Sn_4P_3 compound breaks into small Sn particles and a $K_{3-x}P$ matrix (Figure 8D). Subsequently, K is inserted into Sn to first form K_4Sn_{23} and finally KSn through the alloying
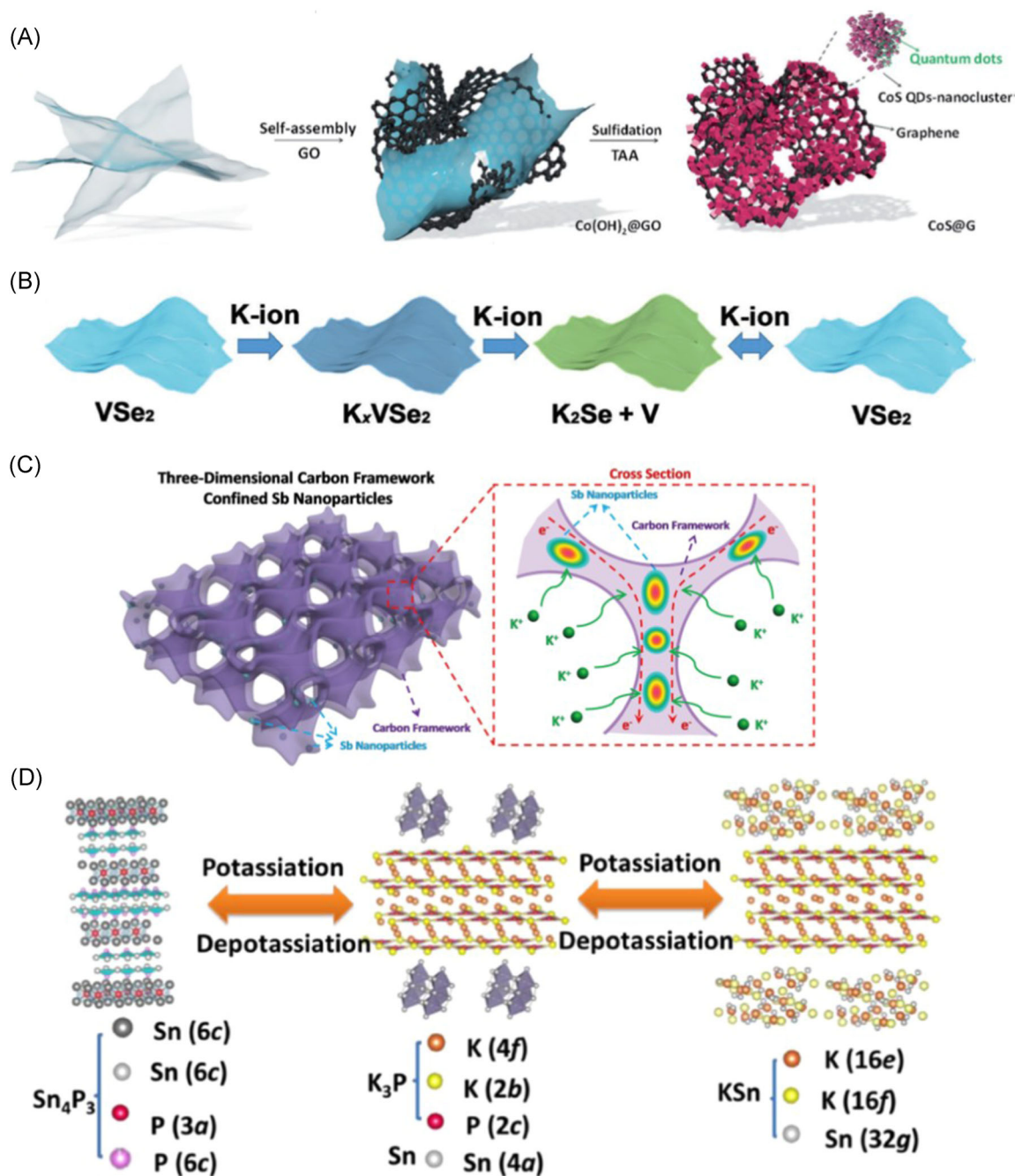
FIGURE 8 A, Schematic illustration of the synthesis process for the CoS@G-25 composite. Reprinted with permission.[77] Copyright 2017, John Wiley and Sons. B, Schematic illustration of the reversible K^+ ion storage in the ultrathin VSe_2 nanosheets. Reprinted with permission.[80] Copyright 2018, John Wiley and Sons. C, Schematic illustration of the 3D SbNPs@C hybrid electrode with large electrode-electrolyte contact area, short K-ion diffusion distances and fast electron transport network. Reprinted with permission.[121] Copyright 2018, The Royal Society of Chemistry. D, Potassiation/depotassiation process in Sn_4P_3/C electrode. Reprinted with permission.[45] Copyright 2017, American Chemical Society

reaction. During the depotassiation, KSn de-alloys first to form Sn, and then Sn reacts with $K_{3-x}P$ to convert it back to Sn_4P_3, thus, the stepped formation of K-Sn (K_4Sn_{23}, KSn) and K-P alloy ($K_{3-x}P$) phases.

Metal Bi can also serve as the anode in KIBs and delivers an excellent capacity of 322 mAh g^{-1} with high

CE of 86.9% after 300 cycles at 2 C.[82] It is found that Bi undergoes three two-phase reactions: Bi ⇌ KBi_2, KBi_2 ⇌ K_3Bi_2, and K_3Bi_2 ⇌ K_3Bi. During this process, the bulk Bi gradually evolved to a 3D porous network, which allows fast K^+ ion transmission and buffers the volume change, thus resulting in the outstanding stability.

Recently, a composite of Bi and N-doped carbon (Bi@N-C) was synthesized through a solvothermal method.[131] The multicore-shell structure has a conductive porous N-doped carbon shell with the nanosized Bi being encapsulated inside. This unique nanostructure not only prevents the volume expansion during the potassiation /depotassiation process but also forms a stable SEI during cycling. As a result, the Bi@N-C exhibits an excellent rate performance of $152 \, \text{mAh g}^{-1}$ at $100 \, \text{A g}^{-1}$ and long cycle life of $203 \, \text{mAh g}^{-1}$ at $10 \, \text{A g}^{-1}$ after 1000 cycles.

2.3 | Organic compounds

Compared with inorganic materials, organic compounds offer several advantages such as good structural controllability, abundant resources, and is cost-effective, which make them one of the most promising anode materials for KIBs.[132-134] Besides this, different from the inorganic solid/crystal constituted by the covalent/ionic bond, the solid/crystal state of organic materials is mainly interacted by van der Waals forces, indicating more void space and low energy barrier for accommodating large K^+ ions.[135]

Para-aromatic dicarboxylic acids such as dipotassium terephthalate (K_2TP) and 2,5-pyridinedicarboxylate (K_2PC) have been designed (Figure 9A).[83,84] The K_2PC anode exhibits a higher discharge capacity of $181 \, \text{mAh g}^{-1}$ at 0.2 C for 100 cycles than that of K_2TP, due to K_2PC possessing a better electron affinity than K_2TP for involving the electron-deficient pyridine ring, which derives from the lowest empty molecular orbital in K_2PC. At the same time, another kind of K_2TP was synthesized via the reaction of terephthalic acid with KOH in aqueous solution (Figure 9B). This K_2TP anode shows a large discharging capacity of $249 \, \text{mAh g}^{-1}$ with CEs of nearly 100% at $200 \, \text{mA g}^{-1}$ after 100 cycles and high capacity retention of 94.6% after 500 cycles at $1000 \, \text{mA g}^{-1}$. The high performance is attributed to the active carboxylate groups, flexible layered molecular structure, and the robust SEI film.

As members of para-conjugated dicarboxylates embedded in biphenyl skeletons, potassium 1,1′-biphenyl-4,4′-dicarboxylate (K_2BPDC) and potassium 4,4′-E-stilbenedicarboxylate (K_2SBDC) were studied as anodes for KIBs (Figures 9C,D).[136] The larger π-conjugated biphenyl skeletons of these two organic compounds are more favorable for intermolecular electron transport than that of the K_2TP. In light of this, remarkable capacities of $120 \, \text{mAh g}^{-1}$ for K_2BPDC and $80 \, \text{mAh g}^{-1}$ for K_2SBDC at $20 \, \text{mA g}^{-1}$ for 100 cycles were achieved, respectively. However, K_2BPDC displays higher rate capacities (105/93/76/52 \, \text{mAh g}^{-1}$) than those of K_2SBDC (74/55/40/26 \, \text{mAh g}^{-1}$) at larger current densities of 50/100/200/500 \, \text{mA g}^{-1}$, as K_2BPDC has a relatively high electronic conductivity compared to that of K_2SBDC. Notably, the capacity of K_2BPDC also achieves excellent cyclic stability of $75 \, \text{mAh g}^{-1}$ at $1 \, \text{A g}^{-1}$ for 3000 cycles.
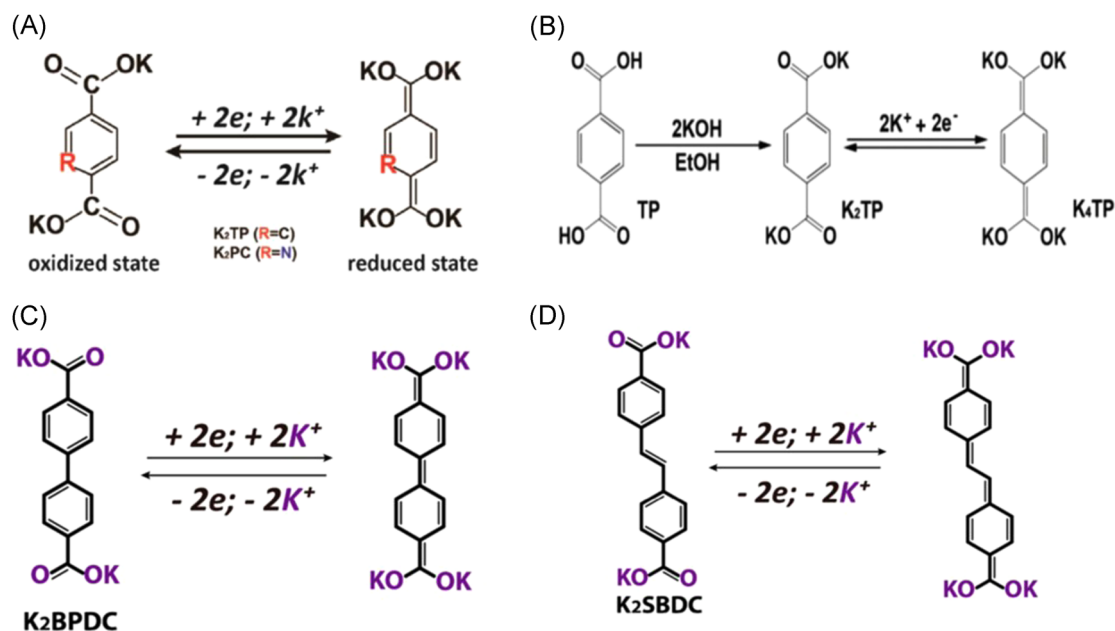
FIGURE 9 A, Illustration of the electrochemical mechanism of K_2TP and K_2PC in potassium-ion batteries. Reprinted with permission.[83] Copyright 2017, Elsevier. B, Schematic illustration of the synthesis and reversible K^+ insertion/extraction of K_2TP. Reprinted with permission.[84] Copyright 2017, The Royal Society of Chemistry. C, Chemical structures of the potassium 1,1′-biphenyl-4,4′-dicarboxylate (K_2BPDC) and (D) the potassium 4,4′-E-stilbenedicarboxylate (K_2SBDC). Reprinted with permission.[135] Copyright 2017, American Chemical Society

3 | CONCLUSION AND PERSPECTIVES

In this review, we have comprehensively summarized recent progress in developing anode materials for KIBs. The strengths and weaknesses of the developed anode materials for KIBs have been elucidated, assessed, and analyzed in detail. Despite the rapid progress in anode material development and significant improvement in KIBs performance achieved, more in-depth research is still necessary to address the capacity and stability of anode materials for KIBs to meet the requirements of KIBs for practical applications.

Among many carbonaceous anode materials, graphite is one of the most promising candidates, owing to its low-cost and mature technology developed in LIBs. More importantly, the stable K^+ ions de/intercalation voltage plateau of graphite is above 0.1 V vs K^+/K to guarantee both high working voltage and high energy density, but it is still imperative to further understand the mechanism of K^+ ions insertion/extraction from graphite as well as the formation and growth of SEI film on the graphite surface. Other carbonaceous materials besides graphite such as HC, soft carbon, and nanostructured carbon materials have also been demonstrated as KIBs anodes with desirable electrochemical performance. In particular, many nongraphite carbons have exhibited high capacities at high current rates even cycling over hundreds of cycles. Nevertheless, the first CE (always less than 60%) and volumetric capacities of these nongraphite carbons still need to be further improved. Noncarbonaceous anodes, such as alloys and conversion electrodes, are also considered as alternatives for the graphite anode attributed to both high gravimetric and volumetric energy density. Apart from that, noncarbonaceous anodes also suffer from huge volume changes during the de/intercalation of large K^+ ions, giving rise to structural failure and rapid capacity decay, thus buffering volume variations is the key point in developing novel noncarbonaceous anode with high capacity. Shape controlling, compositional designing, and functional group modification may be promising solutions. Finally, low-cost organic anode materials have gained much popularity, but further research is still required to solve their solubility issue and relatively low energy density.

To date, many strategies have been proposed to improve the performance of KIBs, including nanostructuring, heteroatom doping, and electrolytes/binder optimizing. Nanostructures generally produce high surface areas, increase the contact area of the electrode and electrolyte, and improve active reaction sites, which can enable fast ion transportation during charging/discharging. For carbon-based materials, heteroatom doping is an effective way to enhance electrical conductivity, enlarge surface reaction sites, and generate defect sites and functional groups, resulting in improving the specific capacity of carbon materials. The aim of optimizing electrolytes/binders is forming stable SEI films, which can reduce the volume expansion and, thus, alleviate pulverization. Another purpose is reducing the solubility of electrode materials in electrolytes and alleviating the decomposition reaction of electrolyte, especially at high voltage.

Overall, it should be admitted that the development of anode materials is still inadequate, and most reported KIBs anodes to deliver an inferior performance compared with LIBs and SIBs. Nevertheless, with improvements in material structure design, the further understanding of the fundamentals of electrochemical behaviors in KIBs, and the exploration of compatible electrolytes and binders, KIBs will become a competitive application in future energy storage systems.

ORCID

Yong Lei http://orcid.org/0000-0001-5048-7433

REFERENCES

1. Barton JP, Infield DG. Energy storage and its use with intermittent renewable energy. *IEEE Trans Energy Convers* 2004; 19(2):441-448.
2. Dincer I. Renewable energy and sustainable development: a crucial review. *Renew Sust Energy Rev.* 2000;4(2):157-175.
3. Johansson TB, Kelly H, Reddy AK, et al. Renewable energy: sources for fuels and electricity. 1993.
4. Zhao H, Liu L, Lei Y. A mini review: functional nanostructuring with perfectly-ordered anodic aluminum oxide template for energy conversion and storage. *Front Chem Sci Eng.* 2018;12(3):481-493.
5. Xu R, Zhao H, Jin H, et al. Scalable fabrication of geometry-tunable self-aligned superlattice photonic crystals for spectrum-programmable light trapping. *Nano Energy.* 2019;58:543-551.
6. Wen L, Xu R, Cui C, et al. Template-guided programmable janus heteronanostructure arrays for efficient plasmonic photocatalysis. *Nano Lett.* 2018;18(8):4914-4921.
7. Xu R, Wen L, Wang Z, et al. Three-dimensional plasmonic nanostructure design for boosting photoelectrochemical activity. *ACS Nano.* 2017;11(7):7382-7389.
8. Wang Z, Cao D, Xu R, Qu S, Wang Z, Lei Y. Realizing ordered arrays of nanostructures: a versatile platform for converting and storing energy efficiently. *Nano Energy.* 2016;19:328-362.
9. Hao Y, Liu Q, Zhou Y, et al. A 2D NiFe bimetallic metal–organic frameworks for efficient oxygen evolution electrocatalysis. *Energy Environ Mater.* 2019;2(1):18-21.
10. Jiang Y, Liu J. Definitions of pseudocapacitive materials: a brief review. *Energy Environ Mater.* 2019;2(1):30-37.

11. Yu F, Li S, Chen W, Wu T, Peng C. Biomass-derived materials for electrochemical energy storage and conversion: overview and perspectives. *Energy Environ Mater*. 2019;2(1):55-67.

12. Hasani A, Teklagne MA, Do HH, et al. Graphene-based catalysts for electrochemical carbon dioxide reduction. *Carbon Energy*. 2020;2(1):1-18.

13. Su Z, Ling HY, Li M, et al. Honeycomb-like carbon materials derived from coffee extract via a "salty" thermal treatment for high-performance Li-I_2 batteries. *Carbon Energy*. 2020;2(1):1-11.

14. Shi Y, Liu G, Jin R, Xu H, Wang Q, Gao S. Carbon materials from melamine sponges for supercapacitors and lithium battery electrode materials: a review. *Carbon Energy*. 2019;1:253-275.

15. Lin X, Sun Q, Doyle Davis K, Li R, Sun X. The application of carbon materials in nonaqueous Na-O_2 batteries. *Carbon Energy*. 2019;1:141-164.

16. Adekoya D, Gu X, Rudge M, et al. Carbon nitride nanofibres with exceptional lithium storage capacity: from theoretical prediction to experimental implementation. *Adv Funct Mater*. 2018;28(50):1803972.

17. Zeng Z, Xu R, Zhao H, et al. Exploration of nanowire-and nanotube-based electrocatalysts for oxygen reduction and oxygen evolution reaction. *Mater Today Nano*. 2018;3:54-68.

18. Yue S, Liu K, Xu R, et al. Efficacious engineering on charge extraction for realizing highly efficient perovskite solar cells. *Energy Environ Sci*. 2017;10(12):2570-2578.

19. Sun Y, Lu S, Xu R, et al. Collection optimization of photo-generated charge carriers for efficient organic solar cells. *J Power Sources*. 2019;412:465-471.

20. Azam M, Yue S, Xu R, et al. Highly efficient solar cells based on Cl incorporated tri-cation perovskite materials. *J Mater Chem A*. 2018;6(28):13725-13734.

21. Wu J, Cao Y, Zhao H, Mao J, Guo Z. The critical role of carbon in marrying silicon and graphite anodes for high-energy lithium-ion batteries. *Carbon Energy*. 2019;1(1):57-76.

22. Nawwar M, Poon R, Chen R, Sahu RP, Puri IK, Zhitomirsky I. High areal capacitance of Fe_3O_4-decorated carbon nanotubes for supercapacitor electrodes. *Carbon Energy*. 2019;1(1):124-133.

23. Larcher D, Tarascon J-M. Towards greener and more sustainable batteries for electrical energy storage. *Nat Chem*. 2015;7(1):19-29.

24. Scrosati B, Hassoun J, Sun Y-K. Lithium-ion batteries. A look into the future. *Energy Environ Sci*. 2011;4(9):3287-3295.

25. Han B, Yang Y, Shi X, et al. Spontaneous repairing liquid metal/Si nanocomposite as a smart conductive-additive-free anode for lithium-ion battery. *Nano Energy*. 2018;50:359-366.

26. Wu T-H, Zhang Y, Althouse ZD, Liu N. Nanoscale design of zinc anodes for high-energy aqueous rechargeable batteries. *Mater Today Nano*. 2019;6:100032.

27. Liu J, Yuan H, Cheng X-B, et al. A review of naturally derived nanostructured materials for safe lithium metal batteries. *Mater Today Nano*. 2019;8:100049.

28. Wu X, Leonard DP, Ji X. Emerging non-aqueous potassium-ion batteries: challenges and opportunities. *Chem Mater*. 2017;29(12):5031-5042.

29. Yabuuchi N, Kubota K, Dahbi M, Komaba S. Research development on sodium-ion batteries. *Chem Rev*. 2014;114(23):11636-11682.

30. Xu Y, Zhou M, Lei Y. Nanoarchitectured array electrodes for rechargeable lithium-and sodium-ion batteries. *Adv Energy Mater*. 2016;6(10):1502514.

31. Sha M, Zhang H, Nie Y, et al. Sn nanoparticles@ nitrogen-doped carbon nanofiber composites as high-performance anodes for sodium-ion batteries. *J Mater Chem A*. 2017;5(13):6277-6283.

32. Xu Y, Zhou M, Lei Y. Organic materials for rechargeable sodium-ion batteries. *Mater Today*. 2018;21(1):60-78.

33. Yang Y, Fu Q, Zhao H, et al. MOF-assisted three-dimensional TiO_2@ C core/shell nanobelt arrays as superior sodium ion battery anodes. *J Alloys Compd*. 2018;769:257-263.

34. Kim H, Kim JC, Bianchini M, Seo DH, Rodriguez-Garcia J, Ceder G. Recent progress and perspective in electrode materials for K-ion batteries. *Adv Energy Mater*. 2018;8(9):1702384.

35. Zhang J, Liu T, Cheng X, et al. Development status and future prospect of non-aqueous potassium ion batteries for large scale energy storage. *Nano Energy*. 2019;60:340-361.

36. Wu X, Chen Y, Xing Z, et al. Advanced carbon-based anodes for potassium-ion batteries. *Adv Energy Mater*. 2019;9(21):1900343.

37. Vaalma C, Buchholz D, Passerini S. Non-aqueous potassium-ion batteries: a review. *Curr Opin Electrochem*. 2018;9:41-48.

38. Eftekhari A, Jian ZL, Ji XL. Potassium secondary batteries. *ACS Appl Mater Interfaces*. 2017;9(5):4404-4419.

39. Dreyer I, Gomez-Porras JL, Riedelsberger J. The potassium battery: a mobile energy source for transport processes in plant vascular tissues. *New Phytol*. 2017;216(4):1049-1053.

40. Recham N, Rousse G, Sougrati MT, et al. Preparation and characterization of a stable $FeSO_4F$-based framework for alkali ion insertion electrodes. *Chem Mater*. 2012;24(22):4363-4370.

41. Taylor S. Abundance of chemical elements in the continental crust: a new table. *Geochim Cosmochim Acta*. 1964;28(8):1273-1285.

42. Kubota K, Dahbi M, Hosaka T, Kumakura S, Komaba S. Towards K-ion and Na-ion batteries as "Beyond Li-Ion". *The Chemical Record*. 2018;18(4):459-479.

43. Liu Y, Tai Z, Zhang J, et al. Boosting potassium-ion batteries by few-layered composite anodes prepared via solution-triggered one-step shear exfoliation. *Nat Commun*. 2018;9(1):3645.

44. Zhang W, Pang WK, Sencadas V, Guo Z. Understanding high-energy-density Sn_4P_3 anodes for potassium-ion batteries. *Joule*. 2018;2(8):1534-1547.

45. Zhang W, Mao J, Li S, Chen Z, Guo Z. Phosphorus-based alloy materials for advanced potassium-ion battery anode. *J Am Chem Soc*. 2017;139(9):3316-3319.

46. Jian ZL, Luo W, Ji XL. Carbon electrodes for K-ion batteries. *J Am Chem Soc*. 2015;137(36):11566-11569.

47. Komaba S, Hasegawa T, Dahbi M, Kubota K. Potassium intercalation into graphite to realize high-voltage/high-power potassium-ion batteries and potassium-ion capacitors. *Electrochem Commun*. 2015;60:172-175.

48. Kim H, Yoon G, Lim K, Kang K. A comparative study of graphite electrodes using the co-intercalation phenomenon for rechargeable Li, Na and K batteries. *ChemComm*. 2016;52(85):12618-12621.

49. Zhao J, Zou X, Zhu Y, Xu Y, Wang C. Electrochemical intercalation of potassium into graphite. *Adv Funct Mater*. 2016;26(44):8103-8110.

50. Xing Z, Qi Y, Jian Z, Ji X. Polynanocrystalline graphite: a new carbon anode with superior cycling performance for K-ion batteries. *ACS Appl Mater Interfaces*. 2016;9(5):4343-4351.

51. An Y, Fei H, Zeng G, et al. Commercial expanded graphite as a low–cost, long-cycling life anode for potassium–ion batteries with conventional carbonate electrolyte. *J Power Sources*. 2018;378:66-72.

52. Vaalma C, Giffin GA, Buchholz D, Passerini S. Non-aqueous K-ion battery based on layered $K_{0.3}MnO_2$ and hard carbon/carbon black. *J Electrochem Soc*. 2016;163(7):A1295-A1299.

53. Jian Z, Hwang S, Li Z, et al. Hard-soft composite carbon as a long-cycling and high-rate anode for potassium-ion batteries. *Adv Funct Mater*. 2017;27(26):1700324.

54. Jian Z, Xing Z, Bommier C, Li Z, Ji X. Hard carbon microspheres: potassium-ion anode versus sodium-ion anode. *Adv Energy Mater*. 2016;6(3):1501874.

55. Tai Z, Zhang Q, Liu Y, Liu H, Dou S. Activated carbon from the graphite with increased rate capability for the potassium ion battery. *Carbon*. 2017;123:54-61.

56. Ju Z, Zhang S, Xing Z, Zhuang Q, Qiang Y, Qian Y. Direct synthesis of few-layer F-doped graphene foam and its lithium/potassium storage properties. *ACS Appl Mater Interfaces*. 2016;8(32):20682-20690.

57. Share K, Cohn AP, Carter R, Rogers B, Pint CL. Role of nitrogen-doped graphene for improved high-capacity potassium ion battery anodes. *ACS Nano*. 2016;10(10):9738-9744.

58. Chen C, Wang Z, Zhang B, et al. Nitrogen-rich hard carbon as a highly durable anode for high-power potassium-ion batteries. *Energy Stor Mater*. 2017;8:161-168.

59. Qi X, Huang K, Wu X, et al. Novel fabrication of N-doped hierarchically porous carbon with exceptional potassium storage properties. *Carbon*. 2018;131:79-85.

60. Ma G, Huang K, Ma JS, Ju Z, Xing Z, Zhuang Q. Phosphorus and oxygen dual-doped graphene as superior anode material for room-temperature potassium-ion batteries. *J Mater Chem A*. 2017;5(17):7854-7861.

61. Adams RA, Syu J-M, Zhao Y, Lo CT, Varma A, Pol VG. Binder-free N-and O-rich carbon nanofiber anodes for long cycle life K-ion batteries. *ACS Appl Mater Interfaces*. 2017; 9(21):17872-17881.

62. Li Y, Adams RA, Arora A, et al. Sustainable potassium-ion battery anodes derived from waste-tire rubber. *J Electrochem Soc*. 2017;164(6):A1234-A1238.

63. Zhao X, Xiong P, Meng J, Liang Y, Wang J, Xu Y. High rate and long cycle life porous carbon nanofiber paper anodes for potassium-ion batteries. *J Mater Chem A*. 2017;5(36): 19237-19244.

64. Wang X, Han K, Qin D, et al. Polycrystalline soft carbon semi-hollow microrods as anode for advanced K-ion full batteries. *Nanoscale*. 2017;9(46):18216-18222.

65. Hao R, Lan H, Kuang C, Wang H, Guo L. Superior potassium storage in chitin-derived natural nitrogen-doped carbon nanofibers. *Carbon*. 2018;128:224-230.

66. Yang J, Ju Z, Jiang Y, et al. Enhanced capacity and rate capability of nitrogen/oxygen dual-doped hard carbon in capacitive potassium-ion storage. *Adv Mater*. 2018;30(4): 1700104.

67. Kishore B, Venkatesh G, Munichandraiah N. $K_2Ti_4O_9$: a promising anode material for potassium ion batteries. *J Electrochem Soc*. 2016;163(13):A2551-A2554.

68. Dong Y, Wu ZS, Zheng S, et al. Ti_3C_2 MXene-derived sodium/potassium titanate nanoribbons for high-performance sodium/potassium ion batteries with enhanced capacities. *ACS Nano*. 2017;11(5):4792-4800.

69. Han J, Xu M, Niu Y, et al. Exploration of $K_2Ti_8O_{17}$ as an anode material for potassium-ion batteries. *Chem Commun*. 2016; 52(75):11274-11276.

70. Han J, Niu Y, Bao S, Yu YN, Lu SY, Xu M. Nanocubic $KTi_2(PO_4)_3$ electrodes for potassium-ion batteries. *ChemComm*. 2016;52(78): 11661-11664.

71. Lian P, Dong Y, Wu ZS, et al. Alkalized Ti_3C_2 MXene nanoribbons with expanded interlayer spacing for high-capacity sodium and potassium ion batteries. *Nano Energy*. 2017;40:1-8.

72. Naguib M, Adams RA, Zhao Y, et al. Electrochemical performance of MXenes as K-ion battery anodes. *Chem Commun*. 2017;53(51):6883-6886.

73. Li P, Zheng X, Yu H, et al. Electrochemical potassium/lithium-ion intercalation into $TiSe_2$: kinetics and mechanism. *Energy Stor Mater*. 2019;16:512-518.

74. Ren X, Zhao Q, McCulloch WD, Wu Y. MoS_2 as a long-life host material for potassium ion intercalation. *Nano Res*. 2017; 10(4):1313-1321.

75. Xie K, Yuan K, Li X, et al. Superior potassium ion storage via vertical MoS_2 "Nano-Rose" with expanded interlayers on graphene. *Small*. 2017;13(42):1701471.

76. Sultana I, Rahman MM, Mateti S, Ahmadabadi VG, Glushenkov AM, Chen Y. K-ion and Na-ion storage performances of Co_3O_4-Fe_2O_3 nanoparticle-decorated super P carbon black prepared by a ball milling process. *Nanoscale*. 2017;9(10): 3646-3654.

77. Gao H, Zhou T, Zheng Y, et al. CoS quantum dot nanoclusters for high-energy potassium-ion batteries. *Adv Funct Mater*. 2017;27(43):1702634.

78. Lakshmi V, Chen Y, Mikhaylov AA, et al. Nanocrystalline SnS_2 coated onto reduced graphene oxide: demonstrating the feasibility of a non-graphitic anode with sulfide chemistry for potassium-ion batteries. *ChemComm*. 2017;53(59):8272-8275.

79. Lu YY, Chen J. Robust self-supported anode by integrating Sb_2S_3 nanoparticles with S,N-codoped graphene to enhance K-storage performance. *Sci China: Chem*. 2017;60(12): 1533-1539.

80. Yang C, Feng J, Lv F, et al. Metallic graphene-like VSe_2 ultrathin nanosheets: superior potassium-ion storage and their working mechanism. *Adv Mater*. 2018;30(27):1800036.

81. Sultana I, Rahman MM, Ramireddy T, Chen Y, Glushenkov AM. High capacity potassium-ion battery anodes based on black phosphorus. *J Mater Chem A*. 2017;5(45):23506-23512.

82. Lei K, Wang C, Liu L, et al. A porous network of bismuth used as the anode material for high-energy-density potassium-ion batteries. *Angew Chem Int Ed*. 2018;57(17):4687-4691.

83. Deng Q, Pei J, Fan C, et al. Potassium salts of para-aromatic dicarboxylates as the highly efficient organic anodes for low-cost K-ion batteries. *Nano Energy*. 2017;33:350-355.

84. Lei K, Li F, Mu C, et al. High K-storage performance based on the synergy of dipotassium terephthalate and ether-based electrolytes. *Energy Environ Sci*. 2017;10(2):552-557.

85. Pramudita JC, Sehrawat D, Goonetilleke D, Sharma N. An initial review of the status of electrode materials for potassium-ion batteries. *Adv Energy Mater*. 2017;7(24):1602911.

86. Rüdorff W, Schulze E. Über Alkaligraphitverbindungen. *Z Anorg Allg Chem*. 1954;277(3-4):156-171.

87. Nixon D, Parry G. Formation and structure of the potassium graphites. *J Phys D* 1968;1(3):291-298.

88. Schleede A, Wellmann M. Notiz über die Herstellung eines Lindemannglases für Kapillaren zwecks Aufnahme von luftempfindlichen Substanzen mit langwelliger Röntgenstrahlung. *Z Kristallogr Cryst Mater*. 1932;83(1-6):148-149.

89. Wang Z, Selbach SM, Grande T. Van der Waals density functional study of the energetics of alkali metal intercalation in graphite. *RSC Adv*. 2014;4(8):4069-4079.

90. Nishitani R, Uno Y, Suematsu H. In situ observation of staging in potassium-graphite intercalation compounds. *Phys Rev B*. 1983;27(10):6572-6575.

91. Nishitani R, Uno Y, Suematsu H, Fujii Y, Matsushita T. In-plane density of potassium liquid and liquid-solid transitions in potassium graphite intercalation compounds. *Phys Rev Lett*. 1984;52(17):1504-1507.

92. Wang Z, Ratvik AP, Grande T, Selbach SM. Diffusion of alkali metals in the first stage graphite intercalation compounds by vdW-DFT calculations. *RSC Adv*. 2015;5(21):15985-15992.

93. Xu Z, Lv X, Chen J, Jiang L, Lai Y, Li J. Dispersion-corrected DFT investigation on defect chemistry and potassium migration in potassium-graphite intercalation compounds for potassium ion batteries anode materials. *Carbon*. 2016;107:885-894.

94. Xu Y, Zhang C, Zhou M, et al. Highly nitrogen doped carbon nanofibers with superior rate capability and cyclability for potassium ion batteries. *Nat Commun*. 2018;9(1):1720.

95. Vaalma C, Giffin GA, Buchholz D, Passerini S. Non-aqueous K-ion battery based on layered K0.3MnO$_2$ and hard carbon/carbon black. *J Electrochem Soc*. 2016;163(7):A1295-A1299.

96. Wang X, Sun G, Routh P, Kim DH, Huang W, Chen P. Heteroatom-doped graphene materials: syntheses, properties and applications. *Chem Soc Rev*. 2014;43(20):7067-7098.

97. Liu Y, Dai H, Wu L, et al. A large scalable and low-cost sulfur/nitrogen dual-doped hard carbon as the negative electrode material for high-performance potassium-ion batteries. *Adv Energy Mater*. 2019;9(34):1901379.

98. Chen M, Wang W, Liang X, et al. Sulfur/oxygen codoped porous hard carbon microspheres for high-performance potassium-ion batteries. *Adv Energy Mater*. 2018;8(19):1800171.

99. Liu Y, Fan F, Wang J, et al. In situ transmission electron microscopy study of electrochemical sodiation and potassiation of carbon nanofibers. *Nano Lett*. 2014;14(6):3445-3452.

100. Share K, Cohn AP, Carter RE, Pint CL. Mechanism of potassium ion intercalation staging in few layered graphene from in situ Raman spectroscopy. *Nanoscale*. 2016;8(36):16435-16439.

101. Wang X, Han K, Wang C, et al. Graphene oxide-wrapped dipotassium terephthalate hollow microrods for enhanced potassium storage. *ChemComm*. 2018;54(78):11029-11032.

102. Luo W, Wan J, Ozdemir B, et al. Potassium ion batteries with graphitic materials. *Nano Lett*. 2015;15(11):7671-7677.

103. Adekoya D, Li M, Hankel M, et al. Design of a 1D/2D C$_3$N$_4$/rGO composite as an anode material for stable and effective potassium storage. *Energy Stor Mater*. 2020;25:495-501.

104. Zhao L, Hu YS, Li H, Wang Z, Chen L. Porous Li$_4$Ti$_5$O$_{12}$ coated with N-doped carbon from ionic liquids for Li-ion batteries. *Adv Mater*. 2011;23(11):1385-1388.

105. Ma Y, Ding B, Ji G, Lee JY. Carbon-encapsulated F-doped Li$_4$Ti$_5$O$_{12}$ as a high rate anode material for Li$^+$ batteries. *ACS Nano*. 2013;7(12):10870-10878.

106. Silva R, Voiry D, Chhowalla M, Asefa T. Efficient metal-free electrocatalysts for oxygen reduction: polyaniline-derived N-and O-doped mesoporous carbons. *J Mater Chem A*. 2013;135(21):7823-7826.

107. Wang C, Guo Z, Shen W, Xu Q, Liu H, Wang Y. B-doped carbon coating improves the electrochemical performance of electrode materials for Li-ion batteries. *Adv Funct Mater*. 2014;24(35):5511-5521.

108. Cao X, Wu J, Jin C, Tian J, Strasser P, Yang R. MnCo$_2$O$_4$ anchored on P-doped hierarchical porous carbon as an electrocatalyst for high-performance rechargeable Li–O$_2$ batteries. *ACS Catal*. 2015;5(8):4890-4896.

109. Yang J, Zhou X, Wu D, Zhao X, Zhou Z. S-doped N-rich carbon nanosheets with expanded interlayer distance as anode materials for sodium-ion batteries. *Adv Mater*. 2017;29(6):1604108.

110. Cao Y, Zhu K, Wu Q, Gu Q, Qiu J. Hydrothermally synthesized barium titanate nanostructures from K$_2$Ti$_4$O$_9$ precursors: morphology evolution and its growth mechanism. *Mater Res Bull*. 2014;57:162-169.

111. Han J, Niu Y, Bao S, Yu YN, Lu SY, Xu M. Nanocubic KTi$_2$(PO$_4$)$_3$ electrodes for potassium-ion batteries. *Chem Commun*. 2016;52(78):11661-11664.

112. Naguib M, Come J, Dyatkin B, et al. MXene: a promising transition metal carbide anode for lithium-ion batteries. *Electrochem Commun*. 2012;16(1):61-64.

113. Er D, Li J, Naguib M, Gogotsi Y, Shenoy VB. Ti$_3$C$_2$ MXene as a high capacity electrode material for metal (Li, Na, K, Ca) ion batteries. *ACS Appl Mater Interfaces*. 2014;6(14):11173-11179.

114. Ling Z, Ren CE, Zhao MQ, et al. Flexible and conductive MXene films and nanocomposites with high capacitance. *Proc Natl Acad Sci USA*. 2014;111(47):16676-16681.

115. Wang X, Kajiyama S, Iinuma H, et al. Pseudocapacitance of MXene nanosheets for high-power sodium-ion hybrid capacitors. *Nat Commun*. 2015;6:6544.

116. Naguib M, Adams RA, Zhao Y, et al. Electrochemical performance of MXenes as K-ion battery anodes. *ChemComm*. 2017;53(51):6883-6886.

117. David L, Bhandavat R, Singh G. MoS$_2$/graphene composite paper for sodium-ion battery electrodes. *ACS Nano*. 2014;8(2):1759-1770.

118. Ge J, Fan L, Wang J, et al. MoSe$_2$/N-doped carbon as anodes for potassium-ion batteries. *Adv Energy Mater*. 2018;8(29):1801477.

119. Adekoya D, Chen H, Hoh HY, et al. Hierarchical Co$_3$O$_4$@N-doped carbon composite as an advanced anode material for ultrastable potassium storage. *ACS Nano*. 2020;14(4):5027-5035.

120. Lakshmi V, Chen Y, Mikhaylov AA, et al. Nanocrystalline SnS$_2$ coated onto reduced graphene oxide: demonstrating the feasibility of a non-graphitic anode with sulfide chemistry for potassium-ion batteries. *Chem Commun*. 2017;53(59):8272-8275.

121. Han C, Han K, Wang X, et al. Three-dimensional carbon network confined antimony nanoparticle anodes for high-capacity K-ion batteries. *Nanoscale*. 2018;10(15):6820-6826.

122. Derrien G, Hassoun J, Panero S, Scrosati B. Nanostructured Sn-C composite as an advanced anode material in high-performance lithium-ion batteries. *Adv Mater*. 2007;19(17):2336-2340.

123. Zhu Z, Wang S, Du J, et al. Ultrasmall Sn nanoparticles embedded in nitrogen-doped porous carbon as high-performance anode for lithium-ion batteries. *Nano Lett*. 2014;14(1):153-157.

124. Li W, Chou SL, Wang JZ, Kim JH, Liu HK, Dou SX. $Sn_{4+x}P_3$ @ amorphous Sn-P composites as anodes for sodium-ion batteries with low cost, high capacity, long life, and superior rate capability. *Adv Mater*. 2014;26(24):4037-4042.

125. Liu Y, Zhang N, Jiao L, Tao Z, Chen J. Ultrasmall Sn nanoparticles embedded in carbon as high-performance anode for sodium-ion batteries. *Adv Funct Mater*. 2015;25(2):214-220.

126. Kim H, Ji H, Wang J, Ceder G. Next-generation cathode materials for non-aqueous potassium-ion batteries. *Trends Chem*. 2019;1:682-692.

127. McCulloch WD, Ren X, Yu M, Huang Z, Wu Y. Potassium-ion oxygen battery based on a high capacity antimony anode. *ACS Appl Mater Interfaces*. 2015;7(47):26158-26166.

128. Zheng J, Yang Y, Fan X, et al. Extremely stable antimony–carbon composite anodes for potassium-ion batteries. *Energy Environ Sci*. 2019;12(2):615-623.

129. Sultana I, Ramireddy T, Rahman MM, Chen Y, Glushenkov AM. Tin-based composite anodes for potassium-ion batteries. *Chem Commun*. 2016;52(59):9279-9282.

130. Wang Q, Zhao X, Ni C, et al. Reaction and capacity-fading mechanisms of tin nanoparticles in potassium-ion batteries. *J. Phys. Chem. C*. 2017;121(23):12652-12657.

131. Yang H, Xu R, Yao Y, Ye S, Zhou X, Yu Y. Multicore-shell Bi@N-doped carbon nanospheres for high power density and long cycle life sodium- and potassium-ion anodes. *Adv Funct Mater*. 2019;29(13):1809195.

132. Park Y, Shin DS, Woo SH, et al. Sodium terephthalate as an organic anode material for sodium ion batteries. *Adv Mater*. 2012;24(26):3562-3567.

133. Zhang P, Yokoyama T, Itabashi O, Suzuki TM, Inoue K. Hydrometallurgical process for recovery of metal values from spent lithium-ion secondary batteries. *Hydrometallurgy*. 1998;47(2-3):259-271.

134. Zou F, Chen YM, Liu K, et al. Metal organic frameworks derived hierarchical hollow NiO/Ni/graphene composites for lithium and sodium storage. *ACS Nano*. 2016;10(1):377-386.

135. Sakaushi K, Hosono E, Nickerl G, et al. Aromatic porous-honeycomb electrodes for a sodium-organic energy storage device. *Nat Commun*. 2013;4:1485.

136. Li C, Xue J, Ma J, Li J. Conjugated dicarboxylate with extended naphthyl skeleton as an advanced organic anode for potassium-ion battery. *J Electrochem Soc*. 2018;166(3):A5221-A5225.

AUTHOR BIOGRAPHIES

Mo Sha received his BS degree (2013) from Jiangnan University and MS degree (2017) in Materials Science and Engineering from Soochow University. He is now a PhD student under the supervision of Prof Yong Lei at the Ilmenau University of Technology. His research interests focus on functional nanostructures for sodium and potassium ion batteries.
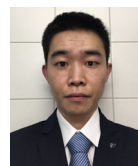
Long Liu received his BS degree (2013) and MS degree (2016) in Material Science from Qingdao University. He is now a PhD student under the supervision of Prof Yong Lei at the Ilmenau University of Technology. His research interests focus on functional nanostructures for supercapacitors and batteries.
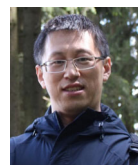
Huaping Zhao received his PhD in Materials Science from the State Key Laboratory of Crystal Materials, Shandong University in 2007. He then worked as a postdoctoral researcher successively at the Institute of Chemistry, Chinese Academy of Sciences, and the University of Muenster from 2007 to 2011. Since 2012, he works as a senior scientist in Prof Yong Lei's group at the Ilmenau University of Technology. His research interests are in the design and fabrication of functional nanostructures for energy storage and conversion applications.

Yong Lei received his PhD at the Chinese Academy of Sciences in 2001. After 2-year postdoc research at Singapore-MIT Alliance, he worked as an Alexander von Humboldt Fellow at Karlsruhe Institute of Technology (2003-2006). Later he worked at the University of Muenster as a group leader (2006-2009) and a Junior Professor (2009-2011). In 2011, he joined the Ilmenau University of Technology as a Professor and the Head of Group of Applied Nano-physics (Fachgebiet Angewandte Nanophysik). His research focuses on template-based nanostructuring, energy-related and optoelectronic applications of functional nanostructures. He received a few prestigious funding including the European Research Council Grant and BMBF (Federal Ministry of Education and Research of Germany) project.